

AD-A179 504

THE STRUCTURE OF TURBULENT VELOCITY FIELDS(U) ARIZONA

1/1

UNIV TUCSON ENGINEERING EXPERIMENT STATION

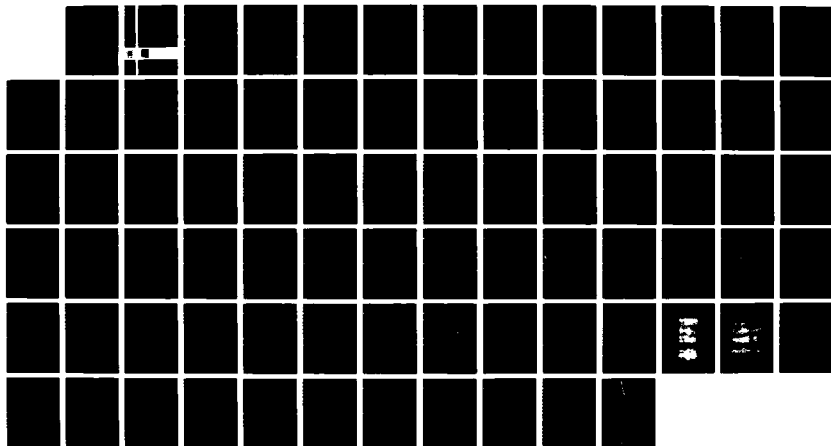
F H CHAMPAGNE ET AL. 09 FEB 85 AFOSR-TR-87-0307

UNCLASSIFIED

F49620-79-C-0224

F/G 20/4

NL



UNCLASSIFIED

SECURITY CLASSIFICATION OF THIS PAGE

A179504

REPORT DOCUMENTATION PAGE

1a. REPORT SECURITY CLASSIFICATION Unclassified		1b. RESTRICTIVE MARKINGS	
2a. SECURITY CLASSIFICATION AUTHORITY		3. DISTRIBUTION/AVAILABILITY OF REPORT Unclassified	
2b. DECLASSIFICATION/DOWNGRADING SCHEDULE			
4. PERFORMING ORGANIZATION REPORT NUMBER(S)		5. MONITORING ORGANIZATION REPORT NUMBER(S) AFOSR-TR-84-0287	
6a. NAME OF PERFORMING ORGANIZATION Engineering Experiment Station College of Engineering	6b. OFFICE SYMBOL (If applicable) N/A	7a. NAME OF MONITORING ORGANIZATION Air Force Office of Scientific Research	
6c. ADDRESS (City, State and ZIP Code) University of Arizona Tucson, Arizona 85721		7b. ADDRESS (City, State and ZIP Code) Bolling Air Force Base, Building 410 Washington, D. C. 20332	
8a. NAME OF FUNDING/SPONSORING ORGANIZATION Air Force Office of Scientific Research	8b. OFFICE SYMBOL (If applicable) AFSC/DA	9. PROCUREMENT INSTRUMENT IDENTIFICATION NUMBER F49620-79-C-0224	
8c. ADDRESS (City, State and ZIP Code) Bolling Air Force Base Building 410 Washington, D. C. 20332		10. SOURCE OF FUNDING NOS.	
		PROGRAM ELEMENT NO. 611C2F	PROJECT NO. 2307
		TASK NO. A2	WORK UNIT NO.
11. TITLE (Include Security Classification) THE STRUCTURE OF TURBULENT VELOCITY FIELDS			
12. PERSONAL AUTHOR(S) F. H. Champagne			
13a. TYPE OF REPORT Final	13b. TIME COVERED FROM 6/1/79 TO 1/31/84	14. DATE OF REPORT (Yr., Mo., Day) 2/9/85	15. PAGE COUNT 78
16. SUPPLEMENTARY NOTATION			
17. COSATI CODES		18. SUBJECT TERMS (Continue on reverse if necessary and identify by block number)	
FIELD	GROUP	SUB. GR.	
		Turbulence; Wakes; Coherent Structures	
19. ABSTRACT (Continue on reverse if necessary and identify by block number)			
<p>A systematic study of two-dimensional, turbulent, small-deficit wakes was carried out to investigate the structure and universality of their self-preserving states. Various wake generators, including circular cylinders, a symmetrical airfoil, a flat plate, and an assortment of screens of varying solidity, were studied for a wide range of downstream distances. The drag coefficient of most generators, and therefore the momentum thickness, was tailored to be identical, permitting comparison at identical Reynolds numbers and aspect ratios. The flat plate and airfoil had a small, trailing-edge flap which could be externally driven to introduce forced sinuous oscillations into the wake. The results indicate that the normalized characteristic velocity and length scales depend on the initial conditions, while the shape of the normalized mean velocity profile is independent of initial conditions or the nature of the generator. The normalized distributions of the longitudinal turbulence intensity, however, are dependent on the initial conditions.</p>			
20. DISTRIBUTION/AVAILABILITY OF ABSTRACT UNCLASSIFIED/UNLIMITED <input checked="" type="checkbox"/> SAME AS RPT. <input type="checkbox"/> OTIC USERS <input type="checkbox"/>		21. ABSTRACT SECURITY CLASSIFICATION Unclassified	
22a. NAME OF RESPONSIBLE INDIVIDUAL JAMES MCMICHAEL		22b. TELEPHONE NUMBER (Include Area Code) 202 767 4435	22c. OFFICE SYMBOL AFOSR/DA

19. ABSTRACT (continued)

Linear inviscid stability theory, in which the divergence of the mean flow was taken into account, predicts quite well the amplification and ~~the~~ transverse distributions of amplitudes and phases of externally imposed sinuous waves on a fully developed turbulent wake generated by a flat plate. There is a strong indication that the large structures observed in the unforced wake are related to the two-dimensional instability modes and therefore can be modelled by linear stability theory. ~~Furthermore, the~~ interaction of the two possible modes of instability may be responsible for the vortex street-type pattern observed visually in the small-deficit, turbulent wake.

Final Technical Report

THE STRUCTURE OF TURBULENT VELOCITY FIELDS

Contract No. F49620-79-C-0224

Prepared for

Air Force Office of Scientific Research
Fluid Mechanics
Bolling Air Force Base
Building 410
Washington, D. C. 20332

by

Francis H. Champagne
Barsam Marasli
Israel Wygnanski

University of Arizona
Department of Aerospace and Mechanical Engineering
Tucson, Arizona 85721

9 FEBRUARY 1985

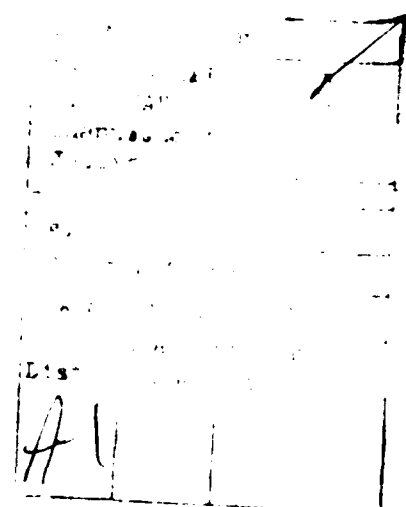


TABLE OF CONTENTS

<u>Section</u>		<u>Page</u>
	REPORT DOCUMENTATION PAGE	iii
1	INTRODUCTION	1
2	EXPERIMENTAL ARRANGEMENT	4
3	THEORETICAL CONSIDERATIONS	7
	3.1 Similarity Conditions	7
	3.2 Linear Stability Analysis	10
4	EXPERIMENTAL RESULTS	14
	4.1 General	14
	4.2 The Universality of the Mean Flow Field in a Small-Deficit, Plane Wake	15
	4.3 The Longitudinal Component of Turbulent Intensity	19
	4.4 Spectra and Normal Modes of Instability	20
	4.5 The Amplification of Imposed Sinuous Oscillations	21
5	DISCUSSION	31
6	CONCLUSIONS	36
	ACKNOWLEDGMENTS	36
	REFERENCES	37
	FIGURE CAPTIONS	39
	LIST OF TABLES	72

1. INTRODUCTION

Turbulent, plane wakes generated by circular cylinders in the absence of a pressure gradient have been the subject of numerous experimental investigations, the most notable of which are those by Townsend (1947, 1949). The results of these studies, along with results obtained in other free shear flows, led to the early ideas of self-preservation and Reynolds number independence proposed by Townsend (1956). It was postulated that, sufficiently far downstream from the cylinder, an asymptotic self-preserving state is achieved for which the flow can be described by a single velocity scale u_0 and a single length scale L_0 (see Figure 1.1). That is, the transverse distributions of mean velocity and Reynolds stress must be independent of the streamwise coordinate x when normalized by these scales. One question under investigation presently is to determine whether and where these scales can be considered unique.

It has been well established (Townsend 1956, Uberoi and Freymuth 1969, Symes and Fink 1977, Yamada et al. 1980) that far-wake flows are self-preserving and that the velocity and length scales, u_0 and L_0 , vary as $(x - x_0)^{-1/2}$ and $(x - x_0)^{1/2}$, respectively, as predicted by the equations of motion and the momentum integral constraint. The virtual origin, x_0 , is used to account for viscous or Reynolds number effects. Furthermore, Townsend (1956) indicated that at sufficiently high Reynolds number, L_0/d and u_0/U_∞ are universal functions of x/d only, where d is the diameter of the cylinder. The initial motivation for the present study stemmed from comparing some early measurements describing the downstream variation of the streamwise component of turbulence intensity. We observed large differences between our data and data reported in the literature that could not be attributed to experimental technique (Figure 1.2). Large differences between the various results are evident, and the trends in the data are quite different at large $x/C_D d$, where C_D is the drag coefficient. At the time (circa 1970), most investigators used the cylinder diameter for the purpose of normalization. Considerations based on the equations of motion show that the momentum thickness, θ , should have been used as the

normalizing length scale for the small-deficit wake. That is, the drag force exerted on the fluid by the cylinder should be used to define the initial flow conditions. We will use 2θ because $C_{Dd} = 2θ$. It can be shown that the normalized velocity and length scales should vary as

$$\left(\frac{U}{u_0} \right)^2 \sim \left(\frac{x - x_0}{2θ} \right) \quad (1.1)$$

$$\left(\frac{L_0}{θ} \right)^2 \sim \left(\frac{x - x_0}{2θ} \right)$$

The data of Townsend (1956), Symes and Fink (1977), and Yamada et al. (1980) confirm the above relations and show that mean velocity profiles observed by each investigator are self-similar when scaled by their individual velocity and length scales. However, comparison of the data indicates a possible lack of universality in the behavior of these scales; that is, different wakes developed at different rates with downstream distance.

Sreenivasan (1981) examined the manner in which wakes produced by a variety of generators approached self-preserving states. He observed substantial differences in the way these flows evolved, even though each flow preserved the shape of the mean velocity profile when normalized by its own characteristic scales. Sreenivasan and Narasimha (1982) suggested that a unique self-preserving state exists for all plane wakes and defined the characteristic constants stemming from their suggestion. We felt at the time that their data did not fully support their conclusion, and the present study compiles further evidence negating it.

One possible explanation for the lack of uniqueness is suggested by the results of Symes and Fink (1977), who investigated the effect of turbulence in the free stream on the development of wakes. They showed that the relative scale of the external turbulence, rather than the level of the turbulence intensity, was an important parameter affecting the

development of the wake. As each experimental facility has its own unique free-stream disturbances, wakes generated in a particular facility may be unique to that facility only. The lack of uniqueness of various small-deficit wake flows might be explained in terms of the instability of the mean velocity profile in the wake.

Flow visualization (Cimbala et al. 1981) revealed that large coherent structures develop far downstream from the wake generator and these are not necessarily related to the vortices shed from the generator. This was sufficient evidence to suggest that the wake, like the mixing layer, contains large-scale coherent structures which may have a wave-like behavior. Traveling, large structures were observed in both laminar (Freymuth 1966) and turbulent (Brown and Roshko 1974, Oster and Wygnanski 1982) mixing layers, and their behavior was explained by an instability mechanism (Michalke 1965, Gaster et al. 1984). The similarity of the patterns occurring in both laminar and turbulent states is not surprising in view of the fact that the instability mechanism is principally inviscid and is controlled by the mean velocity profiles, which are similar in both situations. Gaster et al. computed the amplitude distributions and the phase speeds of traveling waves associated with large coherent structures in the plane turbulent mixing layer, and they obtained very good agreement with experimental results by accounting for the effects of mean flow divergence. The mean velocity profile in the wake is also inviscidly unstable, and its shape is not affected by transition from laminar to turbulent flow, suggesting that a similar analysis could predict the evolution of the large-scale structures in this flow as well.

The stability and transition of a plane wake, generated by a thin plate placed parallel to a uniform flow, was considered by many investigators (e.g., Sato and Kuriki 1961, Mattingly and Criminale 1972, Zabuski and Deem 1971). The analysis in these investigations, however, was always concerned with the immediate neighborhood of the trailing edge, where the velocity deficit was greater than 60 percent of the free-stream velocity. Sato and Kuriki (1961) limited their analysis to a temporal evolution of the instability at one location in the flow, and Mattingly and Criminale (1972) considered the

instability of the wake to natural disturbances in both time and space and concluded that the spatial evolution of a traveling wave gives superior predictions for the disturbance characteristics experimentally observed. The analysis invariably assumed that the flow was parallel and therefore was limited to a prescribed streamwise location in which the width of the wake was defined. The parallel flow assumption represents a severe constraint on predicting growing disturbances in the wake because, in addition to the local width of the flow, the characteristic velocity scale must also change as a result of the divergence.

In contradistinction to the mixing layer, the plane wake is susceptible to both symmetrical (varicose) and antisymmetrical (sinuous) modes of instability. The varicose mode was traditionally disregarded (e.g., Sato and Kuriki 1961) because calculations based on the parallel flow approximations indicated that the most strongly amplified disturbances were sinuous. Data obtained in this investigation attribute the lack of universality of the self-preserving wake, at least partially, to the interaction between the two modes. Certainly, if one is interested in examining the wake over long distances, one cannot neglect the varicose mode of instability.

The scope of the present investigation is limited to the small-deficit wake starting some 100 momentum thicknesses from the generator and extending to 1500 momentum thicknesses downstream. The flow was always incompressible, with free-stream velocities not exceeding 35 m/sec and typical Reynolds numbers of a few thousand.

2. EXPERIMENTAL ARRANGEMENT

The wakes were generated in the University of Arizona wind tunnel facility. The 30-foot-long tunnel is a closed-circuit type built by Kenney Engineering of California and is nearly identical to its counterparts at Tel Aviv University and the University of Southern California. The test section is 2 feet wide, 3 feet high, and 20 feet long. The top and bottom walls, which are adjustable in height, were adjusted to compensate for boundary layer growth and to obtain a zero streamwise pressure gradient. A 30-hp, variable-speed

motor with tachometer generator and a motor controller drives an axial flow fan with variable-pitch blades. The blades were set to their minimum pitch angle to minimize large-scale turbulence generation. In this configuration, the fan easily supplied the necessary range of speeds in the test section required for the present study, that is, 2 to 35 m/sec. The tunnel is equipped with chilled water cooling coils just downstream of the diffuser section and an electric heating unit just upstream of the fan to control the flow temperature. A Minco platinum resistance thermometer, connected to a special bridge and digital panel display unit, allows measurement of the mean temperature of the flow to $\pm 0.05^\circ\text{C}$.

The plenum chamber contains 4-inch-thick hexcell honeycomb, five 20-mesh stainless-steel screens, and a 4-foot-long stilling section. Following this section is the 10:1 contraction section with a fifth-order polynomial contour to insure separation-free acceleration of the flow to the test section. The wake generators were mounted horizontally across the 2-foot span of the test section at a streamwise location 2 feet downstream from the inlet. Measurements of the velocity profile at this plane indicated that the flow was uniform to ± 0.25 percent. The free-stream disturbance level in the streamwise velocity component is approximately 0.03 percent. The free-stream speed was monitored using a pitot tube placed 1 foot below the wake generator and about 2 inches into the flow. The pitot tube was connected to a MKS Baratron pressure transducer unit.

Velocities were measured using a rake of nine Disa 55P01 hot-wire probes connected to Disa 55M01 and 56C01 constant temperature anemometers. The rake, which was 1.75 inches in total height, was used to measure the mean streamwise component of the instantaneous velocity. The rake was mounted on an internal traversing mechanism with a swept-forward, thin extension arm, placing the probes upstream of any region of flow interference caused by the mechanism. The mechanism permitted traversing in the streamwise and vertical directions with resolutions of 0.10 and 0.01 inch, respectively. The anemometer signals were conditioned using buck and gain amplifiers and simple low pass RC

filters with a 6-dB cutoff point at 10 kHz. The conditioned signals were sent directly to the analog-to-digital converter in the data acquisition system. An LSI 11/23 data acquisition/on-line computer system was used for digital signal processing. The major components of the system include an LSI 11/23 microprocessor, a 15-bit A/D converter with 10 channels of simultaneous sample-and-hold circuitry; a dual-density, 125-ips, tape drive; a 160 M-byte hard disk; 256 K-byte static memory; a printer/plotter; two Tektronix 4006 graphic terminals; a Tektronix 4611 hard-copy unit; and a SKYMNK array processor. The multiple channel capability allows simultaneous, continuous sampling of up to 10 channels, with variable sampling frequency up to 10 kHz. The system can be used as a data logger, i.e., to create digital tapes, or as an on-line computer for real-time analysis.

For calibration, the hot wires were placed in the free stream, well outside the wake, along with a pitot tube which was mounted near the rake. The bridge voltage signals and the output of the pressure transducer connected to the pitot tube were sent to the A/D converter. An n th-order polynomial, $U = P_n(E)$, where the independent variable E is the conditioned bridge voltage, was fit to several calibration velocities for each hot wire, thereby providing an overall calibration for each sensor. Whenever the velocity deficits exceeded $0.20 U_\infty$, a second-order polynomial was used; whereas for $u_0 < 0.10 U_\infty$, a linear fit was adopted, speeding on-line computations.

During the course of the experiments, the temperature of the flow was maintained at $\pm 0.10^\circ\text{C}$ of the calibration temperature. The hot wires were continuously checked for drift. The results were sensitive to any minor calibration changes because the maximum velocity deficit was on the order of 5 percent. Generally, 27 to 36 data points were taken to define a mean velocity and turbulence intensity profile.

The wake generators used in the present experiments are described in Table 2.1. The circular cylinders were steel, drill rods and the screens and solid strip were stainless steel. The cylinder, screens, and solid strip were all mounted under adequate tension to insure that the generators were straight and rigid. The screens and solid strip were specially

constructed to have the same momentum thickness as a 2.56-inch-diameter 1.75 mm cylinder at $Re_H = 400$. The aspect ratio b/d was approximately 24 for the narrow cases. To introduce controlled excitations into the wake, a small flap (5 mm in length) was attached to the trailing edge of the flat plate and airfoil. Violin strings were used to connect the downstream edge of each side of the flap to two matched low speakers, one located on each side of the plate just outside the tunnel sidewalls. The speakers were driven in phase at the desired amplitudes and frequencies by an audio amplifier fed by a Krohn Hite function generator. The forcing frequency and amplitude were monitored by a frequency counter and rms meter.

3. THEORETICAL CONSIDERATIONS

3.1. Similarity Conditions

For a developing wake flow sufficiently far from the generator, the transverse distributions of mean velocity and Reynolds stresses are assumed to be self-preserving. That is, these distributions assume functional forms which are independent of x when normalized by the velocity and length scales, u_0 and L_0 , respectively. This can be expressed in the form

$$\begin{aligned} U &= U_\infty + u_0 f(\eta) \\ \bar{u}^2 &= u_0^2 g_{11}(\eta) \\ \bar{u}\bar{v} &= u_0^2 g_{12}(\eta) \\ \bar{v}^2 &= u_0^2 g_{22}(\eta) \\ \bar{w}^2 &= u_0^2 g_{33}(\eta) \end{aligned} \tag{3.1.1}$$

where $\eta = y/L_0$ and u_0 and L_0 are defined in Figure 1.1. In general, u_0 and L_0 will be functions of the following parameters:

$$u_0, L_0 = fcn(x, \rho, u, U_\infty, F, L, d, GEO, u_{FS}^l, NFS, OTHERS) \quad (3.1.2)$$

where

L = span of the wake generator

d = characteristic width of the wake generator

GEO = geometry of the wake generator

u_{FS}^l = amplitude of the free-stream disturbance level

NFS = nature of the free-stream disturbance

F = drag force on the wake generator per unit length

$OTHERS$ = magnitude and nature of any vibration of the wake generator

The conditions under which self-preserving flow is possible can be obtained by substituting the self-preserving distributions into the equations of mean momentum and turbulent kinetic energy and examining the coefficients in the resulting equations. For the small-deficit far wake in the absence of a pressure gradient, i.e., when $u_0/U_\infty \ll 1$, Townsend (1970) obtains the conditions

$$\frac{U_\infty L_0}{u_0^2} \frac{du_0}{dx} \propto \frac{U_\infty}{u_0} \frac{dL_0}{dx} \quad (3.1.3)$$

The self-preserving functions are also subject to the momentum integral constraint

$$\frac{F}{\rho U_\infty^2} = \int_{-\infty}^{\infty} \frac{U}{U_\infty} \left[1 - \frac{U}{U_\infty} \right] dy = \theta \quad (3.1.4)$$

where θ is the momentum thickness. In terms of the self-preserving function, f , this becomes

$$\frac{F}{\rho U_{\infty}^2 \theta} = \frac{u_0 L_0}{U_{\infty}^2 \theta} I_1 - \frac{u_0^2 L_0}{U_{\infty}^2 \theta} I_2 \quad (3.1.5)$$

where

$$I_n = \int_{-\infty}^{\infty} f^n(\eta) d\eta \quad n = 1, 2 \quad (3.1.6)$$

are constants for a given wake flow. For the small-deficit wake, $u_0/U_{\infty} \ll 1$, and therefore the second term in (3.1.5) can be dropped, placing a constraint on the product $(u_0 L_0)$ of the two scales, since in the absence of a pressure gradient, F , θ , and U_{∞} are constants independent of x . Dimensional reasoning, along with the linear part of (3.1.5), indicates the variables F , ρ , and U_{∞} in equation (3.1.2) should appear in the combination $F/\rho U_{\infty}^2$ [see also (3.1.4)]. It can be easily shown from (3.1.3) and (3.1.4) that

$$\frac{u_0}{U_{\infty}} \sim \left[\frac{F}{\rho U_{\infty}^2 (x - x_0)} \right]^{1/2} \sim \left[\frac{\theta}{x - x_0} \right]^{1/2} \quad (3.1.7)$$

and

$$L_0 \sim \left[\frac{F(x - x_0)}{\rho U_{\infty}^2} \right]^{1/2} \sim [\theta(x - x_0)]^{1/2} \quad (3.1.8)$$

where x_0 , the virtual origin, is commonly assumed to depend on the Reynolds number and geometry of the generator. This indicates that θ is the appropriate normalizing length scale.

If a universal self-preserving state exists independent of initial conditions, free-stream disturbances, and other parameters, the normalized distribution functions f and g 's are universal functions and u_0 and L_0 , the normalized velocity and length scales, should vary as

$$\left(\frac{U}{u_0} \right)^2 = A\bar{x} \quad (3.1.9)$$

and

$$\left(\frac{L_0}{\theta} \right)^2 = B\bar{x} \quad (3.1.10)$$

where $\bar{x} = (x - x_0)/2$ and A and B are universal constants. 2θ is used to normalize x here because $2\theta = C_D d$, which is nearly equivalent to normalizing by d for the circular cylinders since $C_D \approx 1$. Townsend (1956) and others used d in presenting their cylinder data.

According to Sreenivasan and Narasimha (1982), equations 3.1.7 and 3.1.8 may be written in the form

$$W = \frac{u_0}{U_\infty} \left(\frac{x}{\theta} \right)^{1/2} \quad (3.1.11)$$

and

$$\Delta = L_0 (x\theta)^{-1/2} \quad (3.1.12)$$

where W and Δ are universal constants, provided the small-deficit, equilibrium wake is independent of initial conditions existing near the generator (see also Narasimha and Prabhu 1972). These parameters are related to the slopes in the relations (3.1.9) and (3.1.10) above. If we define W_0 and Δ_0 by (3.1.11) and (3.1.12), where x is replaced by $x - x_0$, then $A = 2/W_0^2$ and $B = 2\Delta_0^2$.

3.2. Linear Stability Analysis

The propagation of small-amplitude, wavy disturbances in a free shear layer was considered analytically by Bouthier (1972), Crighton and Gaster (1976), and Gaster et al. (1984). Since the analysis applied to the plane wake is identical to that presented in the latter reference, only the governing equations and essential features will be presented here.

The equation of motion considered is inviscid and has the following form:

$$\frac{\partial \Omega}{\partial t} + U \frac{\partial \Omega}{\partial x} + V \frac{\partial \Omega}{\partial y} = 0 \quad (3.2.1)$$

where Ω is the vorticity and U and V represent the velocity components in the x and y directions, respectively. Upon neglecting the nonlinear terms, which are deemed to be small, and assuming that a given mean flow is parallel to the first order of approximation, the solution for the perturbation equation has a general form:

$$\psi = \text{RP} \{ \phi(y) \exp[i(\alpha x - \beta t)] \} \quad (3.2.2)$$

where RP stands for the real part and the eigenfunction $\phi(y)$ is defined by the inviscid form of the Orr-Sommerfeld equation:

$$[U(y) - \beta/\alpha](\phi'' - \alpha^2 \phi) - U''(y)\phi = 0 \quad (3.2.3)$$

in which the primes denote differentiation with respect to y . The wave number α and the disturbance frequency β are eigenvalues determined by the solutions of (3.2.3), which decay exponentially on both sides of the wake. Namely, the boundary conditions are

$$\phi'(\pm\infty) \pm \alpha \phi(\pm\infty) = 0 \quad (3.2.4)$$

Although the divergence of the mean flow may be partially controlled by the stresses resulting from the interaction with the disturbances present, within the realm of the linear approximation, the slowly divergent mean flow is assumed to be prescribed by equations (3.1.1). Since the mean flow is assumed to be known, the conditions of self-preservation are not crucial to the analysis; the only requirement is that the derivatives of the mean stream function ψ with respect to x should be much smaller than the derivatives with respect to y (i.e., the boundary layer approximation applies).

By analogy with the parallel flow problem, the perturbation solution has the form

$$\psi = RP \left\{ A(x) \phi(x, y) \exp \left[i \int_{x_0}^x \alpha(x) dx - \beta t \right] \right\} \quad (3.2.5)$$

where $\alpha(x)$ is a local wave number and the eigenfunction $\phi(x, y)$ changes only slowly with x . Since one expects the correction terms resulting from the slow divergence to be small as well, $\alpha(x)$ and $\phi(x, y)$ at a given streamwise location are still determined locally by equation (3.2.3), for which the mean velocity field $U(x, y)$ is known, and the correction term is defined by

$$A(x) = A_0 \exp \left[- \int_{x_0}^x \frac{N(x)}{M(x)} dx \right]$$

where

$$N(x) = \int_{-\infty}^{\infty} \left\{ \beta \left[\phi \left[\frac{\partial \alpha}{\partial x} + 2i \frac{\partial \phi}{\partial x} \right] + U \left[\frac{\partial \phi''}{\partial x} - 3\alpha^2 \frac{\partial \phi}{\partial x} - 3\alpha \phi \frac{\partial \alpha}{\partial x} \right] \right. \right. \\ \left. \left. + 2i \frac{\partial U''}{\partial x} + U'' \frac{\partial \phi}{\partial x} + V[\phi'''' - \alpha^2 \phi] \right\} \tilde{\phi} dy \right.$$

and

$$M(x) = \int_{-\infty}^{\infty} \{ 2\alpha \beta \phi + U[\phi'' - 3\alpha^2 \phi] - U''\phi \} \tilde{\phi} dy \quad (3.2.6)$$

where $\tilde{\phi}(x, y)$ is the adjoint function of $\phi(x, y)$ given by

$$[U(x, y) - \beta/\alpha][\tilde{\phi}'' - \alpha^2 \tilde{\phi}] + 2U'\tilde{\phi}' = 0 \quad (3.2.7)$$

with the boundary conditions presented by

$$\tilde{\phi}'(\pm\infty) \pm \tilde{\phi}(\pm\infty) = 0 \quad (3.2.8)$$

When the mean velocity profile is symmetrical with respect to the line $y = 0$, the inviscid Orr-Sommerfeld equation admits both symmetrical (varicose) and antisymmetrical (sinuous) modes of disturbances. For parallel flow, one may take advantage of the symmetry and substitute a boundary condition on the centerline for the boundary conditions on one side of the wake,

$$\phi(0) = \tilde{\phi}(0) = 1 \quad (3.2.9)$$

$$\phi'(0) = \tilde{\phi}'(0) = 0$$

for the sinuous mode of disturbance, or

$$\phi(0) = \tilde{\phi}(0) = 0 \quad (3.2.10)$$

$$\phi'(0) = \tilde{\phi}'(0) = 1$$

representing the varicose mode. By virtue of the symmetry, one may usually confine attention to the semi-infinite interval $(0, +\infty)$ in the parallel flow computations.

For a given real frequency β of the disturbance, the complex eigenvalues $\alpha(x)$ and eigenfunctions $\phi(x, y)$ and $\tilde{\phi}(x, y)$ were evaluated at each of the streamwise locations of interest, provided the imaginary part $\alpha_i(x) < 0$ (i.e., the disturbances in the quasi-parallel flow approximation are amplified in the downstream direction), and these solutions were used in determining $\Lambda(x)$. The mean velocity field used in solving equations 3.2.3, 3.2.6, and 3.2.7 was obtained experimentally and was expressed by the exponential distribution

$$\frac{U}{U_\infty} = 1 - \frac{u_0}{U_\infty} \exp[-0.637\eta^2 - 0.056\eta^4] \quad (3.2.11)$$

where U_∞ is the free-stream velocity and $u_0(x)$ and $L_0(x)$ are the velocity and length scales discussed in section 3.1. Despite the fact that the normalized shape of the velocity profile, $f(\eta)$, remained invariant for all wake generators considered, the eigensolutions had to be re-evaluated for each generator separately since $u_0(x)$ and $L_0(x)$ are dependent on the initial conditions, even for the small-deficit wakes.

Sato and Kuriki (1961) considered the temporal evolution of the small-amplitude, sinuous disturbance at a single location in the flow at which $(1 - U_0/U_\infty) = 0.692$. Mattingly and Criminale (1972) extended these calculations to both modes of instability evolving spatially and temporally at five prescribed locations in the immediate vicinity of the trailing edge of a flat-plate, wake generator for which $0.44 \leq u_0/U_\infty < 0.692$. Since these computations are strongly dependent on u_0/U_∞ , the solutions obtained are of little value in predicting the character of the amplified disturbances in the small-deficit wake for which $u_0/U_\infty \ll 1$. Furthermore, the assumption of parallel mean flow (i.e., the constancy of u_0/U_∞ and of L_0/θ) led to the general belief that the varicose mode has a negligible effect on the flow because its rate of amplification ($-\alpha_i$) is smaller. It will be shown later that the interaction between the two modes of instability leads to physically acceptable flow patterns associated generally with large coherent structures contained in the wake, in spite of the presence of the small-scale turbulence, which was not considered in the calculations.

4. EXPERIMENTAL RESULTS

4.1. General

The mean flow field in the self-preserving region of a wake and the intensity of the longitudinal component of the turbulent fluctuations were measured for a variety of two-dimensional wake generators. Data were obtained at distances ranging from 100 to 2000

momentum thicknesses downstream of the generator, where typical velocity deficits on the centerline of the wake varied from $0.15 U_\infty$ to $0.03 U_\infty$. The velocity at which the measurements were done varied from 7 to 20 m/sec, corresponding to a range of Reynolds numbers based on the momentum thickness and the kinematic viscosity of air of 650 to 3200. In most instances, the shape and the size of the wake generator were tailored to provide a constant momentum thickness. The effects of Reynolds number and aspect ratio were examined separately in wakes generated by circular cylinders. Forced sinuous disturbances were generated in the wake of a symmetrical airfoil (having a maximum thickness to chord ratio of 30 percent) and a flat plate (thickness to chord ratio of 2 percent) by an oscillating, small flap mounted at the trailing edge. The results are summarized in Table 4.1.

4.2. The Universality of the Mean Flow Field in a Small-Deficit, Plane Wake

The wake investigated most extensively in the literature is generated by a circular cylinder, and therefore our investigation started with this wake generator. Some 400 momentum thicknesses downstream, the velocity scale u_0 was indeed proportional to $\bar{x}^{-1/2}$ and the width of the wake L_0 was proportional to $\bar{x}^{1/2}$, suggesting that similarity of the mean flow was indeed attained. The mean velocity profiles were plotted in the similarity coordinates and collapsed quite neatly onto a single curve described by the exponential function

$$f(\eta) = \exp[-0.637\eta^2 - 0.056\eta^4] \quad (4.2.1)$$

(Figure 4.2.1). The exponential function traditionally used to describe the mean velocity profile (i.e., $f(\eta) = \exp[-0.693\eta^2]$) overestimates the mean velocity measured at the outer edges of the wake and, therefore, the fourth-order correction term was added. We expected the flow to be independent of Re when all length scales were normalized by the

momentum thickness, and indeed the values of W_0 and Δ_0 were not affected by changes in Re ranging from $Re_d = 1360$ to $Re_d = 5900$. The aspect ratio of the cylinder was varied from 96 to 384 by changing the diameter of the cylinder and keeping the span constant (i.e., the distance between the sidewalls of the wind tunnel). The two-dimensionality of the mean flow field was checked at $\bar{x} = 430$ by comparing velocity and turbulence intensity profiles obtained at $z/L_0 = 0 \pm 7.5$ and was found to be satisfactory. The values of $W_0 = 1.75$ and $\Delta_0 = 0.287$ fitted quite well all wakes generated by a circular cylinder (the values were averaged over experimental points with $\bar{x} > 200$). This result would give credence to the universal equilibrium concept suggested by Sreenivasan and Narasimha (1982), except that the asymptotic values of the constants suggested by these authors were quite different, i.e., $W_0 = 1.63$ and $\Delta_0 = 0.300$.

The universality of the mean velocity profile generated by a circular cylinder in our facility could lead to the conclusion that either the development of the plane, small-deficit wake is not susceptible to external disturbances or the velocity-dependent external disturbances in our wind tunnel (like the fan blade passage frequency, vibrations, etc.) are negligible within the range of variables considered. In order to check the validity of either statement, we proceeded to investigate wakes produced by a variety of two-dimensional generators. The first family of generators considered were screens with solidity ratios ranging from 30 to 100 percent (a thin metal strip placed normal to the free stream). The porous screens have numerous advantages: (i) there is no flow reversal in the vicinity of the generator with all its ensuing experimental complications; (ii) the porous screens do not generate vortices in the same way as does the circular cylinder and, therefore, their drag should not be as sensitive to Reynolds number; (iii) the roll-up of vortices in the mixing layers generated in the neighborhood of the screens is, in principle, predictable and dependent on the solidity (Gaster et al. 1984); and (iv) the drag of screens having a different solidity can easily be equated by altering the size of the screens. It was decided to maintain the momentum thickness of all four screens constant in order to avoid any

questions about the unknown effects of Reynolds number or aspect ratio in the development of the plane, small-deficit wake. The shape of the normalized mean velocity profile is identical to that obtained for the circular cylinder in all cases considered, yet the values of W_0 range between 1.67 for the 70 percent solidity screen to 1.88 for the limiting case representing the solidity of 100 percent.

The value of W_0 decreases with increasing solidity of the screens, provided the porosity suffices to prevent flow reversal in the lee of the screen; however, the value of W_0 for the solid strip (which is regarded as a screen having 100 percent solidity) is higher than the value of W_0 for the most porous screen investigated (solidity of 30 percent). This result is attributed to the observed alternate shedding of vortices from the two separation points on the strip. The determination of the threshold solidity beyond which an alternate shedding of vortices starts to occur is not within the scope of the present investigation.

In the absence of periodic forcing, the lowest W_0 measured in this experiment was attained in the wake of a nonlifting, thick, symmetrical airfoil section. The mean velocity field in the wake of the flat plate was quite similar to the velocity field produced by the wake of a circular cylinder except for the location of the virtual origin x_0 . The introduction of periodic surging reduced the effective W_0 from 1.71 to 1.32 without affecting the overall drag experienced by the body (i.e., the product $W_0 \Delta_0$). The location of the virtual origin moved downstream with increasing amplitude of the forced oscillations (Table 2.1).

The product $W_0 \Delta_0$ represents the conservation of momentum within the context of the linearization and, therefore, its constancy for all wake generators ($W_0 = 0.507 \pm 0.002$) reaffirms the suggestion that the normalized shape of the mean velocity profile (Figure 4.2.1) is universal for all the wake generators considered. An example of the variation of $(U_\infty/u_0)^2$ with \bar{x} is shown in Figure 4.2.2, which establishes that $(U_\infty/u_0)^2 = A\bar{x}$ and that the coefficient of proportionality A depends on the wake generator.

The mean velocity in the wake obeys the similarity scaling for $\bar{x} > 200$. The different slopes of the lines drawn in Figure 4.2.2 result in a diversity of estimates for W_0 (Figure 4.2.3), varying between 1.3 and 1.9 depending on the wake generator. The differences are large and are not attributable to experimental inaccuracy.

Only one value of x_0 was chosen for each wake generator, and it had to satisfy the dependence of both U_0 and L_0 on initial conditions. The choice of x_0 does not affect the dependence of W_0 or Δ_0 on the initial conditions, although the absolute values of W_0 and Δ_0 may vary slightly if improper values of x_0 were used. Figure 4.2.3 demonstrates this point. The open symbols refer to physical distances measured from the trailing edge of the generator (i.e., $x_0 = 0$), and therefore the values of W_0 based on these data define a sloping curve rather than a horizontal line. This effect is particularly severe whenever x_0 is large, as it is in the wake of a circular cylinder. It is apparent, therefore, that for the range of distances considered, the mean flow in the plane, small-deficit, turbulent wake is dependent on the initial conditions set up by the generator.

The preservation of momentum deficit in the wake produced by all the generators considered above is illustrated by plotting θ/L_0 versus u_0/U_∞ (Figure 4.2.4). For similar velocity profiles,

$$\frac{\theta}{L_0} = \frac{u_0}{U_\infty} \left[I_1 - \frac{u_0}{U_\infty} I_2 \right] \quad (4.2.2)$$

with I_n as defined in equation 3.1.6.

Equation 4.2.2 describes a parabola (a solid curve in Figure 4.2.4), while the linear approximation $(\theta/L_0)(U_\infty/u_0) = I_1$ is drawn as a dotted line. The values of I_1 and I_2 are 2.06 and 1.505, respectively, and are in excellent agreement with the data of Sreenivasan and Narasimha (1982). Measured values of θ/L_0 follow quite clearly the parabolic curve for all $u_0/U_\infty < 0.14$. The product $(\theta/L_0)(U_\infty/u_0)$ is approximately 1.97 (rather than $I_1 = 2.06$) and represents the shortcoming of the linearization. It is surprising, therefore, that

u_0 and L_0 behave as they do ($u_0 \sim x^{-1/2}$ and $L_0 \sim x^{1/2}$), in spite of the fact that data shown in Figure 4.2.4 illustrate a consistent deviation from the linear approximation.

4.3. The Longitudinal Component of Turbulent Intensity

For a self-preserving wake (Townsend 1956), the longitudinal component of the turbulent intensity u is given by

$$\bar{u}^2 = u_0^2 g_{11}(\eta) \quad (4.3.1)$$

where $g_{11}(\eta)$ supposedly is a universal function analogous to $f(\eta)$. Since the measured distribution of $g_{11}(\eta)$ consistently showed a larger degree of scatter than $f(\eta)$, a normalized function $\bar{u}^2/(\bar{u}^2)_{\max} = G(\eta)$ (4.3.2) was plotted in Figure 4.3.1. The normalized function was used because of the possibility that a slightly erroneous u_0 , resulting from drift in the response of the hot wire, might cause the apparent scatter in $g_{11}(\eta)$. The distributions of \bar{u}^2 plotted in Figure 4.3.1 were measured in the wakes generated by the airfoil, the solid strip, and the 70 percent solid screen. Although each distribution is approximately self-similar (if one is willing to disregard the excessive scatter in the data), the function $G(\eta)$ clearly depends on the type of generator. A good measure in assessing the lack of universality is the ratio $\bar{u}_{CL}^2/\bar{u}_{\max}^2$ (where the subscript CL refers to the center plane of the wake), which varies from 0.73 for the solid strip to 0.9 for the airfoil. This ratio is correlated with the rate of spread of the wake or the decay of the mean velocity on its centerline. Indeed, the lack of universality of \bar{u}_{CL}^2 presented by various investigators for the circular cylinder triggered the present investigation (Figure 1.2). The peculiar shape of $G(\eta)$, which has a local minimum at $\eta = 0$, is associated with a single row of large vortices distributed on the centerline of the wake (see also Wygnanski et al. 1979). It was, therefore, anticipated that large coherent structures which retain their characteristic shape and associated velocity perturbation are responsible for the apparent dependence of the wake on the conditions at its origin.

4.4. Spectra and Normal Modes of Instability

Spectra of the streamwise component of the velocity fluctuations were measured at several \bar{x} locations in the wake behind the flat plate. The measurements presented in Figure 4.4.1 were taken on the centerline at $102 < \bar{x} < 587$, while the spectra in Figure 4.4.2 were measured along a curve representing the outer boundary of the wake, i.e., at $n = 3$. Only the most significant decade of the spectra have been plotted. The abscissa on these figures is frequency plotted on a logarithmic scale, while the ordinate is $fF(f)$ in order to represent the relative contribution to the streamwise component of intensity at a given frequency f [i.e., $\bar{u}^2 \approx \int F(f)df = \int fF(f)d(\log f)$].

The spectra measured on the centerline of the wake (Figure 4.4.1) have a shape which is typically observed in any unbounded, turbulent, shear flow (Champagne 1973). The spectral distribution is broad, and the frequency range associated with the most energetic eddies gradually moves toward lower frequencies as the flow develops in the downstream direction. The insert in Figure 4.4.1 shows a log-log plot of the normalized (to unity) spectra $F(f)$. The frequency has been rendered non-dimensional using the local length scale, L_0 , and U_∞ . The similarity of the spectral distribution indicates that the length scales associated with the energy-containing eddies ($\lambda = U_\infty/f$) are proportional to the width of the wake L_0 and, therefore, L_0 is the appropriate characteristic length scale for use in rendering the mean velocity field self-similar for a given generator.

The spectral measurements at $n = 3$, shown in Figure 4.4.2, represent fluctuations induced by the passage of the large turbulent structures in the wake since the coordinate $n = 3$ is located outside the turbulent interface. The insert in this figure shows that, as with the centerline spectra, these spectra also scale with the local width L_0 . Note the shift of the spectral peaks toward lower frequency with increasing \bar{x} .

Equation (3.2.3) was solved for the prescribed local mean velocity field and numerous real frequencies to obtain the variation of the spatial rate of amplitude ($-\alpha_1$) with

increasing distance from the flat plate. The results of these computations indicate that the maximum local amplification rate shifts toward lower frequencies with increasing \bar{x} . Figure 4.4.3 shows the spatial amplification rates for different frequencies. The value of \bar{x} for which a constant frequency line intercepts the \bar{x} axis (i.e., $\alpha_i = 0$) corresponds to the downstream location at which a wave at that frequency has undergone a maximum of amplification according to parallel, linear, inviscid stability theory. A plot of these intercept values versus frequency, shown also in Figure 4.4.3, gives what we will refer to as the expected predominant frequency in the wake versus distance from the flat plate. The measured predominant frequency range, defined as those frequencies at $n = 3$ whose amplitude is within 90 percent of the peak energy value, are plotted in Figure 4.4.3 and compared with the computed results. The dashed lines show the measured predominant frequency range similarity determined for $n = 0$. The good agreement between the measured predominant frequencies associated with the passage of the large coherent structures and the most-amplified frequencies calculated using parallel flow, linear stability theory suggests that the large structures observed in this flow may be related to the two-dimensional instability modes.

4.5. The Amplification of Imposed Sinuous Oscillations

Two-dimensional sinusoidal oscillations in the direction normal to the mean motion were generated in the wake by the motion of a small flap hinged to the trailing edge of the flat plate. The frequency of the imposed oscillation was matched to the expected most-amplified fluctuations measured at $n = 3$ in the region of interest. A typical power spectrum measured with and without forcing is presented in Figure 4.5.1. Small-amplitude oscillations do not affect the turbulent intensity in the wake nor do they affect the shape of the spectral distribution. The two spectra presented in Figure 4.5.1 are almost identical with the exception of the peak corresponding to the frequency of forcing.

In order to be sure that the instability mechanism in the wake is actually responsible for the amplification of the imposed oscillations, measurements of spectra were repeatedly taken at one location in the flow for a variety of forcing frequencies while all other controlled variables were unchanged. Since the background turbulence level is not affected by the introduction of forcing (Figure 4.5.1), the ratio of the amplitudes between the imposed wave and the background exhibits the sensitivity of the wake to the imposed sinusous perturbations. The normalized spectrum in the center of Figure 4.5.2 shows the ratio of amplitudes for the most-amplified frequency at the location considered. When the frequency of forcing was either higher or lower than the most-amplified frequency for the given location and flow conditions, the ratio between the peak amplitude and the background diminished. In view of the symmetry of the response around the most-amplified frequency (Figure 4.5.2), which was repeated at other flow conditions (and therefore other frequencies), the possibility of resonance of the mechanical flap system was discarded.

The amplitude and phase of an artificially excited sinusous wave at a frequency corresponding to $f\theta/U = 6.4 \times 10^{-3}$ ($f = 20$ Hz) were calculated for the wake of the flat plate. The mean flow required for the solution of eqs. 3.2.3, 3.2.6, and 3.2.7 was provided by eq. 4.2.1 and Table 4.1 (i.e., $W_0 = 1.57$, $\Delta_0 = 0.323$, $\bar{x}_0 = 48$). These equations were solved at intervals of $\bar{x} = 10$ for a rectangular window starting at $\bar{x} = 250$ and ending at $\bar{x} = 750$ and at intervals of 0.1 between $0 \leq y/2\theta \leq 40$. For a given frequency ($\beta = 2\pi f L_0(\bar{x} = 750)/U_\infty$), the eigenvalues $\alpha(x)$ and eigenfunctions $\phi(x, y)$ and $\tilde{\phi}(x, y)$ were evaluated at each of the 51 streamwise locations. These functions, their derivatives with respect to both x and y coordinates, and the mean flow information were used to determine the correction term for slowly divergent flow $A(x)$ (eq. 3.2.6). Only the streamwise component of the velocity perturbation was measured and compared with the calculations.

A typical distribution of normalized amplitudes of the sinusous mode across the entire wake is shown in Figure 4.5.3. The solid line represents computed values, while the triangles represent experimental results at $\bar{x} \sim 500$. The data were acquired by recording

the velocity, together with the sinusoidal signal activating the flap. The velocity signal was phase averaged over 300 cycles of the flap motion, and the Fourier transform of these average records provided the phase and amplitude estimates of the spectral elements of the velocity field, which were quite free from the random, turbulent fluctuations present in the original signals. There is little doubt that the artificially excited wave train can be described by an inviscid linear model, in spite of the fact that the flow is fully turbulent. One may note that the measured amplitude distribution in Figure 4.5.3 is not symmetrical about the centerline; the lack of symmetry is partly attributed to interference between the probe holder and traversing mechanism and the large structures in the wake.

A detailed comparison between the predicted amplitude distribution of the forced wave and measured amplitude profiles at eight streamwise locations is shown in Figure 4.5.4. In the bottom part of this figure, the velocities were normalized by their respective maxima, which are replotted at the top. The computed maximum amplitude at $\bar{x} = 700$ was assigned the value of unity, which is the only floating constant in this comparison. The predicted and measured lateral distributions of amplitudes are in good agreement with one another, as is the decay of the maxima with increasing distance from the generator. It was surprising, at first, to note that the maximum amplitude of the forced wave actually diminished with \bar{x} , in spite of the fact that the quasi-parallel solutions based on eq. 3.2.2 would predict amplification ($\alpha_i < 0$). The reasons for the apparent anomaly stems from the fact that α_i is a small negative number in the range of distances considered, and it is outweighed by the shape of the eigenfunction whose maximum amplitude diminishes with increasing \bar{x} (Figure 4.5.5). A similar observation for an axisymmetric jet was made by Strange (1982). The value of the integral of the perturbation amplitude across the wake increases somewhat with increasing \bar{x} because the width of the wake increases. In fact, the product of the maximum amplitude and the local width is nearly constant between $\bar{x} = 325$ and $\bar{x} = 700$. This result could not have been predicted by the parallel flow

distribution of u^2 shown in Figure 4.3.1, although the ratio $[(\bar{u}_f^2)_{CL}/(\bar{u}_f^2)_{max}]$ is generally lower than the corresponding broad-band distribution. Because the data are no longer phase locked, the actual amplitudes plotted are much larger than for the imposed wave train (Figure 4.5.3). Since the calculated amplitudes do not vanish on the centerline of the wake as predicted by the sinuous mode of inviscid amplification, another mechanism has to be considered. A hint was provided by the fact that the amplification rates $(-\alpha_i)$ predicted on the basis of the parallel flow approximation were overwhelmed by the presence of longitudinal gradients in the mean flow. It seems plausible that the same longitudinal mean flow gradients may have enhanced the relative importance of the varicose mode, which would contribute to the amplitude of the fluctuations on the centerline; if not, non-linear effects and secondary instabilities may have to be considered.

The calculating procedure outlined in section 4.4 was repeated for $f\theta/U_\infty = 1.3 \sim 10^{-2}$ and the appropriate mean flow parameters (Table 4.1). The calculations were done twice; once for the sinuous motion, then a second time for the varicose mode. By assuming that, to the first order of approximation, one may simply superimpose the effects of both modes of instability, the resulting amplitudes can be calculated. For the purpose of comparison between computations and experiment, it was assumed that the initial amplitudes resulting from both modes are equally important; namely, that the maximum amplitude of the varicose mode is equal to the maximum amplitude of the sinuous mode at some initial \bar{x} distance from the generator. The results of these calculations are plotted in Figure 4.6.2 for $370 \leq \bar{x} \leq 640$; the symbols in the figure represent data calculated from experimental results and filtered at $f\theta/U_\infty = 1.3 \sim 10^{-2}$. There is a qualitative agreement between the predicted and measured lateral distributions of the \bar{u}_f^2 amplitudes, indicating that both modes of instability are probably present and can give rise to the peculiar profile of the u fluctuations in the wake. The agreement between theory and experiment in this case is not as good as for the forced sinuous wave, suggesting that either the two-dimensional

approximation is not of value or the simple linear superposition of both modes is inadequate. Another possible error stems from the nonlinear terms neglected in the present context.

In order to explore further the importance of the interaction between the two modes of instability, we resorted to flow visualization using a smoke wire. The wire was positioned at $\bar{x} = 350$, while the camera was located at $\bar{x} = 500$. The smoke patterns were photographed at $U_{\infty} = 3.4$ m/sec ($Re_0 = 600$). Large coherent structures are clearly visible (Figure 4.6.3), even in the absence of any imposed oscillations. These structures are similar in appearance to the Karman vortex street because they seem to be comprised of vortices of alternating sign of vorticity, which are placed in a staggered manner on both sides of the wake centerline. Therefore, neither the varicose mode, which requires that the vortices appear in pairs distributed symmetrically about the centerline, nor the sinuous mode, which requires vortices whose center coincides with the centerline, dominates this flow. Although the vortices are large and coherent and have a prevailing wavelength of approximately 15 cm, there is sufficient irregularity in their shape, size, and position to cause the spectrum of the induced fluctuation at the edge of the wake to be fairly broad (Figure 4.4.2). The introduction of periodic forcing did not have a significant effect on the shape and scales of the large eddies visualized in this manner. The degree of two-dimensionality of these structures was first estimated by placing the smoke wire parallel to the circular cylinder but displacing it from the generator in the lateral direction in order that the smoke would not be entrained by the wake before $\bar{x} = 300$. The resulting photo (Figure 4.6.4) indicates that the large eddies have a tendency to be two dimensional, although the two-dimensionality is by no means perfect. There appears to be a variation of amplitudes along the span of the wake, as well as phase irregularities.

Coherence spectra calculated from u fluctuations sensed by two probes separated in the spanwise direction provide a quantitative measure of the two-dimensionality of the various scales. The two-point, cross-correlation function for stationary random variables $u_j(\underline{x}, t)$ and $u_j(\underline{x} + \underline{r}, t + \tau)$ is defined as

$$R_{ij}(\underline{x}, \underline{r}, \tau) = \overline{u_i(\underline{x}, t) u_j(\underline{x} + \underline{r}, t + \tau)} \quad (4.6.1)$$

and the cross-spectrum,

$$\phi_{ij}(\underline{x}, \underline{r}; f) = \frac{1}{2\pi} \int_{-\infty}^{\infty} R_{ij}(\underline{x}, \underline{r}; \tau) e^{i2\pi f\tau} d\tau = C_{ij}(\underline{r}, \underline{x}; f) - iQ_{ij}(\underline{x}, \underline{r}; f) \quad (4.6.2)$$

where C_{ij} is called the cospectrum and Q_{ij} , the quadrature spectrum. The coherence spectrum is defined as

$$\text{Coh}_{ij}(\underline{x}, \underline{r}; f) = \frac{C_{ij}^2(\underline{x}, \underline{r}; f) + Q_{ij}^2(\underline{x}, \underline{r}; f)}{F_{ii}(\underline{x}; f) F_{jj}(\underline{x} + \underline{r}; f)} \quad (4.6.3)$$

where $F_{ii}(\underline{x}; f)$ and $F_{jj}(\underline{x} + \underline{r}; f)$ are the familiar (one-point) energy spectra, i.e.,

$$\bar{u}_i^2(\underline{x}) = \int_{-\infty}^{\infty} F_{ii}(\underline{x}; f) df \quad (4.6.4)$$

The phase angle θ_{ij} can be obtained as

$$\theta_{ij}(\underline{x}, \underline{r}; f) = \tan^{-1} \left[\frac{Q_{ij}}{C_{ij}} \right] \quad (4.6.5)$$

The coherence spectrum is bounded, and its value must be between 0 and 1. We will consider the component $\text{Coh}_{11}(\underline{x}, \underline{\Delta z}; f)$, which represents the degree of spatial correlation between the Fourier components of $u_1(\underline{x}, t)$ and $u_1(\underline{x} + \underline{k}\Delta z, t + \tau)$ at the same frequency, where \underline{k} is a unit vector in the z or spanwise direction.

A spanwise rake of six hot-wire probes with Δz spacing from 1.1 to 2.54 cm was used for the coherence data. Measurements were taken in the wake of the flat plate with and

without forcing at $\bar{x} = 430$ and 646, with the rake located at $\eta = 0, 0.6$, and 3. The lateral position $\eta = 0.6$ corresponds roughly to the position of maximum u activity. The wake response at $\bar{x} = 646$ and $\eta = 0.6$ to various forcing levels is shown in Figure 4.6.5 for two Δz spacings, 1.1 and 25.4. The values of the coherence at the forcing frequency (50.0 Hz) and its first and second harmonics as a function of amplitude are presented. All amplitudes are scaled by the highest amplitude of forcing. Where the relative forcing amplitude was less than 0.25, the coherence spectrum responded in a linear manner. For amplitudes in the range of 0.25 to 0.5, the value of the coherence at the forcing frequency is nearly independent of Δz in the range investigated, at least up to $\Delta z/L_0 = 10$. The relative amount of energy tied up with the forcing frequency can be determined from the spectrum of the velocity fluctuations. For this case, the spectral peak at 50 Hz was one order of magnitude above the "background" turbulent fluctuation.

Figure 4.6.6 shows the coherence spectra measured at $\bar{x} = 646$, $\eta = 0.6$, and $\Delta z/L_0 = 0.4$, with and without forcing. The forcing frequency was 50 Hz, corresponding to the expected predominant frequency at this \bar{x} , and the relative amplitude of forcing was 0.25. The effect of forcing sharply enhances the value of the coherence at the forcing frequency to 0.92, with little effect on the rest of the spectrum. The corresponding data for $\Delta z/L_0 = 10$ are shown in Figure 4.6.7(a), where only the data for the forced case are presented. The coherence for the unforced case at this separation vanished at all frequencies. For the forced case, the entire correlation is contained in the spectral spike at 50 Hz, for which the coherence is 0.87. Similar results were obtained at forcing levels as low as 0.05, where the peak correlation was 0.21 at 50 Hz. At $\eta = 3$ [Figure 4.6.7(b)], a much higher coherence at the forcing frequency was measured (0.98), indicating that the large structure in the wake must be highly two dimensional to generate such a result for the large spanwise separation, $\Delta z/L_0 = 10$. For the unforced case, the

coherence is nearly zero from 10 to 260 Hz. The results indicate that a slight amount of forcing generates a strong two-dimensional wave in the wake at the forcing frequency.

Is the proposed model capable of explaining the large structures observed in Figure 4.6.3? For this purpose, some streak-lines had to be calculated. Since the calculations were aimed at a qualitative understanding of this phenomenon, a parallel flow approximation was invoked locally. It was assumed that the particles were uniformly released at $\bar{x} = 300$, where $u_0/U_\infty = 0.06$. The prevailing wavelength gave rise to $\beta = 0.8$, which corresponds to the spatially most-amplified sinuous wave train in this mean flow. Both u and v components of the perturbation velocity were calculated across the entire wake, and the corresponding particle paths were established from the equations

$$\frac{dx}{dt} = U[x(t), y(t), t]; \quad \frac{dy}{dt} = V[x(t), y(t), t] \quad (4.6.6)$$

(For a detailed description of the procedure, see Michalke 1965.) The coefficient of velocity perturbation in all these calculations was taken as 0.025.

Five of the streak-lines calculated taking only the sinuous mode into consideration are shown in Figure 4.6.8(a). The streak-lines have a sinusoidal pattern undulating about the centerline of the wake. The amplitude of the undulations increases with increasing distance from the source; at large distances, most of the particles congregate at the outer edge of the wake.

The corresponding, most strongly amplified varicose mode has a perturbation frequency of $\beta = 0.5$ and, therefore, corresponds to $5/8$ of the frequency of the prevailing sinuous mode (not quite a subharmonic frequency). The computed streak-lines for the varicose mode are shown in Figure 4.6.8(b). The particles in this figure congregate in lumps, which are symmetrical about the centerline of the wake. The streak-lines shown in Figure 4.6.8(a) or 4.6.8(b) bear no resemblance to the observed coherent structures seen in Figure 4.6.3.

The streak-lines shown in Figure 4.6.8(c) represent the combined motion of both modes of instability when the coefficient of the velocity perturbation is still maintained at 0.025. The initial ratio between the amplitudes of u and v in the varicose mode and the sinuous mode was 0.7. (This number simply appeared because the eigenfunctions were not normalized; changing the initial ratio by a factor of two made no substantial difference in the pattern.) The initial phase relation between the modes was assumed to be zero. (Changing this number also had no effect on the basic pattern at some distance downstream from the source location.)

The prevailing wavelength of the streak-lines [Figure 4.6.8(c)] still corresponds to the prevailing wavelength of the sinuous mode, but the presence of the varicose mode not only modulates the streak-lines but also contributes to an apparent chaotic behavior. Most important is the fact that these streak-lines, when replotted on a larger scale, resemble the pattern observed in the smoke photographs (Figure 4.6.3). Namely, the particles congregate in a staggered manner about the centerline and the large eddies are, at times, separated by deep incursions of "potential" fluid. Sometimes, these incursions are narrow (marked by the letter "N" in Figure 4.6.9) and, sometimes, they are wide (marked by "W"). Therefore, it transpires that only the combination of both modes can successfully describe the flow.

The distributions of vorticity for the three cases considered in Figure 4.6.5 were calculated directly from the eigenfunctions solved, because the vorticity perturbation

$$\omega(y) = -[U''/(U - \beta/\alpha)]\phi \quad (4.6.7)$$

and the total vorticity

$$\Omega(x, y, t) = -U' + 0.015 \text{ RP}[\omega(y) \exp[i(\alpha x - \beta t)]] \quad (4.6.8)$$

which is, of course, periodic in time. The vorticity contours plotted in Figure 4.6.10 were

calculated for $t = 2\pi/8$ and for $355 \leq \bar{x} \leq 385$, as in Figure 4.6.9. (The shaded regions correspond to negative vorticity.) By neglecting either the varicose mode [Figure 4.6.10(a)] or the sinuous mode [Figure 4.6.10(b)], the resulting vorticity contours appear to be very regular. The contours are either symmetrical or antisymmetrical about the centerline and indicate intensification of vorticity with increasing \bar{x} . The vorticity contours resulting from the combined two modes of instability [Figure 4.6.10(c)] are surprisingly similar to the contours produced by the sinuous mode alone. One may notice, however, that the intensity of the contours in Figure 4.6.10(c) are modulated by the varicose mode, even if they are not severely distorted by the addition of this mode. A simple superposition of Figure 4.6.10(c) on Figure 4.6.8 leads to the conclusion that a congregation of particles observed in a still photograph does not necessarily correspond to a concentration of vorticity.

5. DISCUSSION

The velocity and length scales in a plane, turbulent, and supposedly self-preserving wake are dependent on initial conditions and, therefore, on the shape and size of the obstacle generating the wake. We could not prove that these scales will not become universal functions of (x/θ) at extremely large values of (x/θ) , but the distances at which this may (or may not) occur may be so large as to have no practical impact on the problem since the range of x/θ values in the present study extended to 2000 where $u_0/U \sim 0.03$. The dependence of the plane mixing layer on initial conditions was observed some years ago (Champagne et al. 1976) and traced to the presence of large coherent structures (Oster and Wygnanski 1982). The existence of large coherent structures in a wake, however, was often confused with vortex shedding, which was so ably discussed by Karman (1912) in the lee of a circular cylinder at low Reynolds numbers. The large eddies proposed by Townsend (1956) and Grant (1958) bear little resemblance to the structures observed presently.

Townsend suggested that the large eddies present in fully turbulent free shear flows might be generated by hydrodynamic instability of the mean flow.

What is the cause for the apparent dependence of the small-deficit wake on the shape of the generator? The nature of the flow in the vicinity of the generator, including any vortices shed by the generator, can provide the only plausible explanation for this phenomenon. The frequency, amplitude, and predominant mode of the initial perturbation vary from one geometry to another. For all geometries investigated, the predominant mode of shedding was sinuous, but the presence of the varicose mode was also detected in the vicinity of the low-solidity screens and circular cylinder. The strongest sinuous oscillations were observed downstream of the thick symmetrical airfoil because the initiation of separation from one surface changed the circulation around the airfoil, moving the front stagnation point toward the separated surface and therefore initiating a separation from the opposite surface. The amplitude at the shedding frequency was three orders of magnitude stronger than the background turbulence. The amplitude of the oscillations behind a circular cylinder of screens was approximately two orders of magnitude above the background, while the amplitude of the oscillations downstream of the solid strip held normal to the flow was of the same order of magnitude as the background.

It is also suspected that the lower the frequency of the shedding, the more persistent the initial effects will be; in fact, the frequency of shedding downstream of the symmetrical airfoil of a given thickness depends on the chord length, provided the flow separates upstream of the trailing edge. The effects of frequency, however, appear to be less significant than the effects of amplitude. A detailed investigation of the near wake has been undertaken in order to determine the effects of initial condition more precisely.

Cimbala et al. (1981) observed, with the aid of a smoke wire, the evolution of large coherent structures in a wake of a circular cylinder up to $Re_D < 2000$ and in a wake of two screens at comparable Re . These structures became apparent some 200 diameters downstream of the cylinder and had a regular frequency two to three times lower than the

Strouhal frequency. They were unable, however, to corroborate their results with spectral measurements for their high Reynolds number case and attributed it to the high turbulence level in their tunnel. Some measurements of spectra at the outer edge of the wake were presently carried out for two wake generators: (i) a circular cylinder at $Re_\theta = 2500$ corresponding to $Re_d = 5000$ and (ii) a screen having 45 percent solidity, also at $Re_\theta = 2500$. In the immediate neighborhood of the cylinder, the predominant spectral peak (not shown) corresponded to the shedding frequency of the cylinder, i.e., at $St_d = 0.206$ or $St_\theta = 0.10$. At $\bar{x} > 50$, the predominant spectral peak dropped quite abruptly to $St_\theta = 0.03$. Thereafter, the evolution of the spectral peak was rather slow and is hardly detectable on the scale shown in Figure 5.1. The spectral peaks associated with the screen tailored to produce the same momentum thickness as the circular cylinder are similar to those mentioned above at $\bar{x} > 250$. The big difference between the two flows occurs at $50 < \bar{x} < 250$, where the characteristic frequency of the spectral peaks generated by the screen decreases slowly with \bar{x} . At $\bar{x} > 150$, one may detect the appearance of an additional peak in the spectrum, which roughly corresponds to the spectral peak in the far wake of the circular cylinder; this peak amplifies quickly and dominates the spectrum at $\bar{x} > 200$. It seems that the coherent structures in the near wake of this particular screen retain some of their characteristics up to $\bar{x} = 250$, while in the wake of the circular cylinder, this transition is accomplished at $\bar{x} = 50$. It is believed that the shear layers generated in the wake of the screen (see insert in Figure 5.1) undergo an instability process reminiscent of the plane mixing layer (Caster et al. 1984), generating eddies whose characteristic frequency decreases in the downstream direction. Whether these eddies grow by entraining fluid from the surrounding stream or by a process of amalgamation remains to be seen.

Since Cimbalá et al. (1981) did not observe any vortex amalgamation in their visualization experiments, one would be inclined to think that the gradual decrease in the characteristic frequency stemming from an increase in the wavelength of these eddies is caused by entrainment. In any event, once the scale of these eddies becomes comparable

to the width of the screen, an interaction between two shear layers of opposing vorticity has to occur before the wake will become "fully developed". It is possible that a phase accommodation ensues, resulting in a slow evolution of the typical large structures existing in the self-preserving region. The evolution of the fully developed wake is currently being investigated, but the importance of initial conditions is evident in Figure 5.1.

The mutual interaction between the large coherent structures and the mean flow is outside the scope of the linear stability theory. However, the dependence of the mean flow field on the initial conditions, and consequently on the large coherent structures, poses precisely such a problem. The notion that the free-stream turbulence and the shape of the generator may have an effect on the development of a self-preserving wake was proposed by Symes and Fink (1977). These authors observed that the wake generated by a rectangular cylinder did not evolve in the same manner as the wake generated by a circular cylinder, but the most important observation was that the evolution of the wake was sensitive to grid turbulence, whose integral scale was an order of magnitude larger than the scale of the generator. This suggested that the externally imposed turbulence interacted with the flow far downstream, where the typical scales in the wake and in the free stream became comparable. It also implied that an instability mechanism might be responsible for this result. The present investigation confirmed this notion, although nonlinear terms should be considered in order to assess the interaction between the mean flow and the imposed oscillation. Perhaps, an integral approach similar to the one used by Ko et al. (1970) might predict such an interaction through the Reynolds stress. The concept of flow equilibrium and self-preservation has to be carefully reconsidered in view of the present findings, in spite of the fact that the normalized shape of the mean velocity profile was not affected. The dependence of the lateral distribution of \bar{u}^2 on the nature of the generator (Figure 4.3.1) and the relatively poor collapse of the dimensionless data onto a single $G(\eta)$ function for a given wake generator raise the possibility that the flow is not in equilibrium. Although this possibility was considered remote at the start of this investigation, a plot

showing the difference between the maximum intensity $(\bar{u}^2)_{\max}$ and the intensity on the centerline of the wake $(\bar{u}^2)_{CL}$ normalized by u_0^2 is shown in Figure 5.2 for the wake of the flat plate. If the flow was in perfect equilibrium, then $(\bar{u}^2)_{\max} - (\bar{u}^2)_{CL}/u_0^2$ should have been constant at all \bar{x} . Although this plot is very susceptible to experimental inaccuracies and should be treated with due caution, the lack of constancy might have been caused by the modulation by the varicose mode of the vortices resulting from the sinuous mode of instability. The possible interaction between the two modes has to be investigated in detail by considering additional components of the turbulent stress tensor.

The assumption of parallel flow (eq. 3.2.2) makes the eigenfunction $\phi(y)$ and the eigenvalues α and β invariant with respect to streamwise distance from the generator. Thus, for $\alpha_i = 0$ (i.e., spatially amplified waves), only a single mode containing the largest $|\alpha_i|$ need be considered. However, the amplification rates in the small-deficit, plane wake are so small that one cannot disregard one mode of instability in favor of another simply because its $|\alpha_i|$ is the largest. This is so because the long distances required for an unstable wave to amplify increase the relative significance of the longitudinal gradients in the mean velocity. By neglecting the varicose mode in favor of the sinuous one, Sato and Kuriki (1961) had to resort to nonlinear effects in their attempt to explain the cause for the generation of two rows of vortices. Mattingly and Criminale (1972) offered an alternate explanation, which is based on the vorticity distribution of the sinuous mode being superposed on the mean vorticity. The generation of a vortex structure reminiscent of a Karman vortex street can quite easily be attributed to the superposition of the two instability modes, keeping in mind that the most unstable frequency of the varicose mode is only slightly higher than a subharmonic of the most unstable sinuous mode. Sinuous forcing of the flow has little effect on the shape of the large eddies visualized by smoke until the amplitude of the forcing becomes exceedingly high. In this case, the smoke pattern is more regular and the eddies are located closer to the centerline than in the corresponding unforced wake.

6. CONCLUSIONS

It was experimentally observed that the characteristic velocity and length scales, u_0 and L_0 , when suitably scaled by the momentum thickness and the free-stream velocity, do not exhibit universal behavior and do depend on the initial conditions and therefore on the geometry of the wake generator. The mean velocity profiles for each wake, when normalized by their own velocity and length scales, are self-preserving and are also identical for all wake generators. The distributions of the longitudinal turbulence intensity normalized in the same manner are self-preserving, but are not identical, and depend on the geometry of the wake generator.

Linear inviscid stability theory, in which the divergence of the mean flow was taken into account, predicts quite well the amplification and the transverse distributions of amplitudes and phases of externally imposed sinuous waves in a fully developed turbulent wake generated by a flat plate. It appears that the large, coherent, vortex structures occurring naturally in a wake can be modeled by linear stability theory. Furthermore, the interaction of the two possible modes of instability may be responsible for the apparent Karman vortex street-type of structures observed visually in the small-deficit, turbulent wake.

ACKNOWLEDGMENTS

The project was supported by the Air Force Office of Scientific Research under Contract No. F 49620-79-C-0224. I. Wygnanski would like to express his thanks to AFOSR for providing the opportunity for him to devote his entire sabbatical stay to this project. The authors would like to thank Dr. M. Gaster, who provided the initial impetus for the theoretical approach.

REFERENCES

- Bouthier, M., 1972, J. Mecanique, 11, 599.
- Brown, G. L. and A. Roshko, 1974, J. Fluid Mech., 64, 775.
- Champagne, F. H., 1978, J. Fluid Mech., 86, 67.
- Champagne, F. H., Y. H. Pao and I. J. Wygnanski, 1976, J. Fluid Mech., 74, 209.
- Cimbala, J., H. Nagib and A. Roshko, 1981, Bull. Am. Phys. Soc., Series II, 2.
- Crighton, D. G. and M. Gaster, 1976, J. Fluid Mech., 77, 297.
- Freytmuth, P., 1966, J. Fluid Mech., 25, 683.
- Gaster, M., E. Kit and I. Wygnanski, 1984, J. Fluid Mech., to be published.
- Grant, H. L., 1958, J. Fluid Mech., 4, 149.
- Karman, Th. v., 1912, Nachr. Ges. Wiss. Gottingen, 547.
- Ko, D. R. S., T. Kubota and L. Lees, 1970, J. Fluid Mech., 40, 315.
- Marasli, B., 1983, Master's Thesis, AME Dept., Univ. of Arizona.
- Mattingly, G. E. and W. O. Criminale, 1972, J. Fluid Mech., 51, 233.
- Michalke, A., 1965, J. Fluid Mech., 23, 521.
- Narasimha, R. and A. Prabhu, 1972, J. Fluid Mech., 54, 1.
- Oster, D. and I. Wygnanski, 1982, J. Fluid Mech., 123, 91.
- Sato, H. and K. Kuriki, 1961, J. Fluid Mech., 11, 321.
- Sreenivasan, K. R., 1981, AIAA Journal, 19, 1365.
- Sreenivasan, K. R. and R. Narasimha, 1982, J. Fluids. Engr. 104, 167.
- Strange, P. J. R., 1982, Ph.D. Thesis, University of Leeds.
- Symes, C. R. and L. E. Fink, 1977, in "Structures and Mechanisms of Turbulence I",
proceedings, Berlin, p. 86.
- Townsend, A. A., 1947, Proc. Roy. Soc., A190, 551.
- Townsend, A. A., 1949, Aust. J. Sci. Res., 2, 451.

Townsend, A. A., 1956, 'The Structure of Turbulent Shear Flow,' 1st Ed., Cambridge University Press, London.

Townsend, A. A., 1970, 'The Structure of Turbulent Shear Flow,' 2nd Ed., Cambridge University Press, London.

Uberoi, M. S. and P. Freymuth, 1969, Phys. Fluids, 12, 1359.

Wynanski, I., D. Oster and H. Fiedler, 1979, in 'Proc. 2nd Symp. on Turbulent Shear Flows,' London, p. ??.



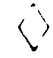
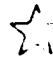
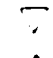


Yamada, H., Y. Kawata, H. Osaka and Y. Kageyama, 1980, Tech. Reports of the Yamaguchi Univ., Japan, 2, No. 4.

Zabuski, N. J. and G. S. Deem, 1971, J. Fluid Mech., 47, 353.

FIGURE CAPTIONS




1.1 A sketch defining the nomenclature.

1.2 Centerline turbulence intensity for wakes generated by circular cylinders.

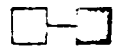
-  Marasli (1983), $Re = 1360$, $AR = 384$
-  Marasli, $Re = 5900$, $AR = 128$
-  Townsend (1977), $Re = 1360$, $AR = 240$
- Townsend (1949)
- Uberoi and Freymuth (1969), $Re = 4320$, $AR = 192$
-  Yamada et al. (1980), $Re = 4000$, $AR = 80$
-  Champagne (1978), $Re = 19,000$, $AR = 32$
-  Symes and Fink (1977), $Re = 6666$, $AR = 150$
-  Symes and Fink, ext. turb.

4.2.1 The shape of the self-similar mean velocity profile. Data from 70 percent solidity screen for $2.0 < \bar{x} < 700$.

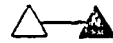
4.2.2 The variation of u_0 with \bar{x} for three wake generators.

-  Airfoil
-  70 percent solidity screen
-  Solid strip

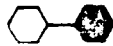
4.2.3 The variation of W_0 with u_0/U for three wake generators.



Airfoil



70 percent solidity screen



Solid strip

4.2.4 The dependence of θ/L_0 on u_0/U_∞ . Symbols represent data from all wake generators studied.

4.3.1 Normalized turbulence intensity distributions for three generators.

4.4.1 Spectra of u fluctuations on centerline of flat-plate wake at various downstream positions. Insert shows similarity of spectra when scaled by L_0 and U_∞ .

4.4.2 Spectra of induced u fluctuations at $\eta = 3$ in the flat-plate wake at various downstream locations. Insert shows similarity of spectra when scaled by L_0 and U_∞ .







4.4.3 Spatial amplification rates computed for several disturbance frequencies in a wake. Insert shows expected predominant frequency (computed) compared to measured predominant frequency range as a function of \bar{x} .

4.5.1 The effect of forcing on the measured u spectrum at $\bar{x} = 400$.

4.5.2 The effect of forcing frequency on the velocity spectrum at a fixed location in the wake. $\bar{x} = 400$.

- 4.5.3 Amplitude distribution of u fluctuations phase locked to the external sinusoidal forcing signal. $\bar{x} = 400$.
- 4.5.4 A comparison between the measured and predicted u perturbation amplitude distributions at several \bar{x} locations in a sinusoidally forced wake. A is not $A(x)$ of theory.
- 4.5.5 The variation of the computed eigenfunction with \bar{x} .
- 4.5.6 A comparison between measured and predicted phase distributions in a wake.
- 4.6.1 The amplitude distribution of the u component $f = 40$ Hz and $\bar{x} = 587$ in the unforced wake.
- 4.6.2 A comparison between measured and predicted u amplitude distributions at several \bar{x} locations in an unforced wake. A is not $A(x)$ of theory.
- 4.6.3 Large coherent structures photographed in the wake of the flat plate with no forcing. $\bar{x} \approx 500$ and $Re_0 = 600$.
- 4.6.4 The spanwise coherence of the large eddies in the wake of a circular cylinder at $\bar{x} \approx 600$ and $Re_0 = 600$.

4.6.5 The response of the wake to various sinusous forcing levels. $\bar{x} = 646$ and $n = 0.6$.

-  $f = 50 \text{ Hz}, \Delta z/L_0 = 10$
-  $f = 50 \text{ Hz}, \Delta z/L_0 = 0.4$
-  $f = 100 \text{ Hz}, \Delta z/L_0 = 10$
-  $f = 100 \text{ Hz}, \Delta z/L_0 = 0.4$
-  $f = 150 \text{ Hz}, \Delta z/L_0 = 10$
-  $f = 150 \text{ Hz}, \Delta z/L_0 = 0.4$

4.6.6 Coherence spectra measured at $\bar{x} = 646$, $n = 0.6$, and $\Delta z/L_0 = 0.4$ in the wake of the flat plate. Upper trace without forcing. Lower trace with forcing at 50 Hz.

4.6.7 (a) Coherence spectrum measured at $\bar{x} = 646$, $n = 0.6$, and $\Delta z/L_0 = 10$, with forcing at 50 Hz.



(b) Same as (a) except $n = 3$.

4.6.8 Streak-lines computed assuming spatial instability of parallel flow at $\bar{x} = 300$:
(a) sinuous, most-amplified mode; (b) varicose, most-amplified mode; (c) combined modes.

4.6.9 Streak-lines from Figure 4.6.8(c) plotted on larger scale to show staggered nature of particle congregation.

4.6.10 Vorticity perturbation contours computed for the three cases of streak-lines shown in Figure 4.6.8: (a) sinuous, most-amplified mode; (b) varicose, most-amplified mode; (c) combined modes.

5.1 The measured predominant frequencies in the wake of:

- (a)  A circular cylinder, $Re_\theta = 2000$
- (b)  The 30 percent solidity screen, $Re_\theta = 2000$.

5.2 The variation of turbulent intensity defect on the centerline of the wake of a flat plate.

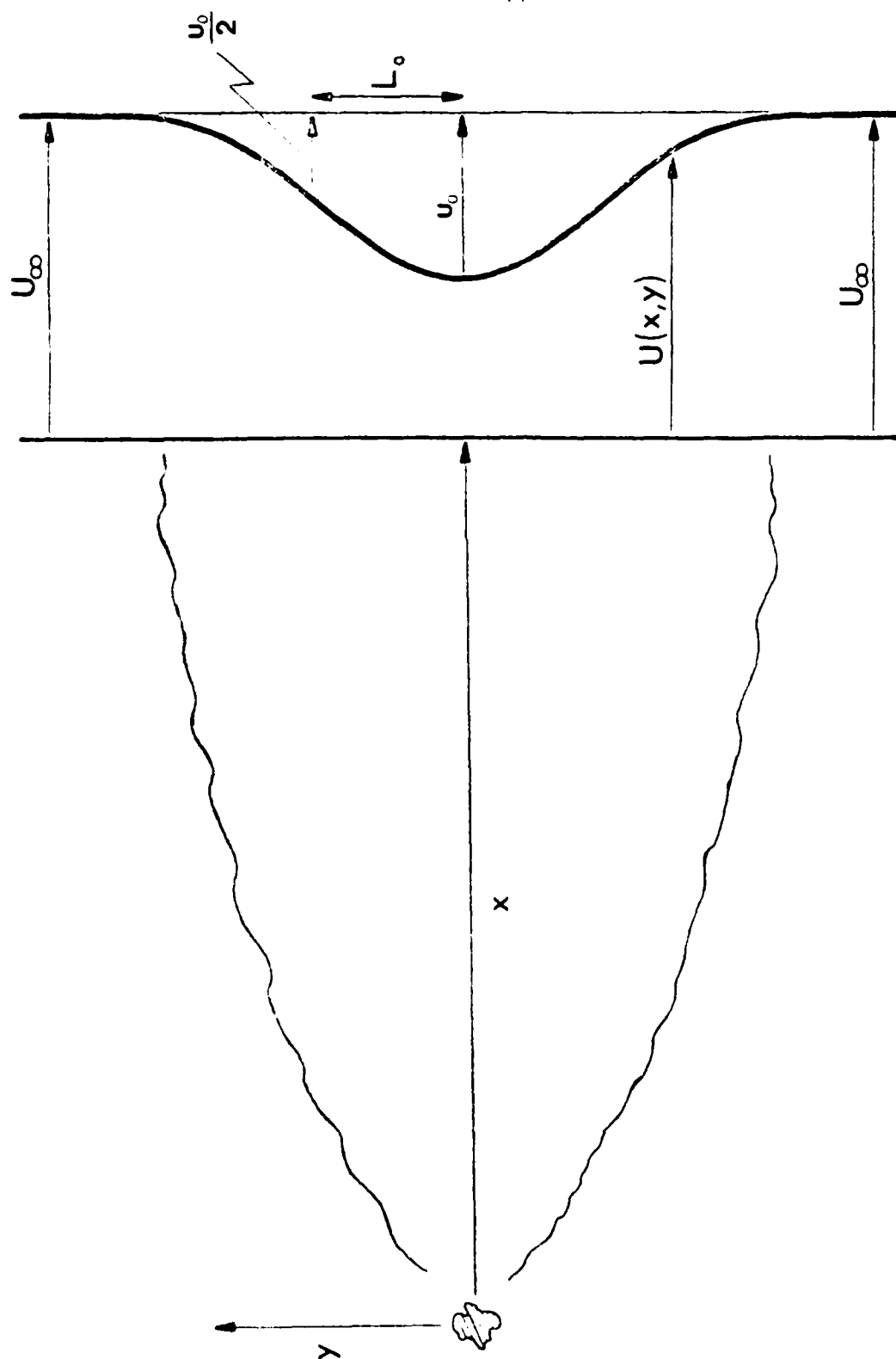


Figure 1.1

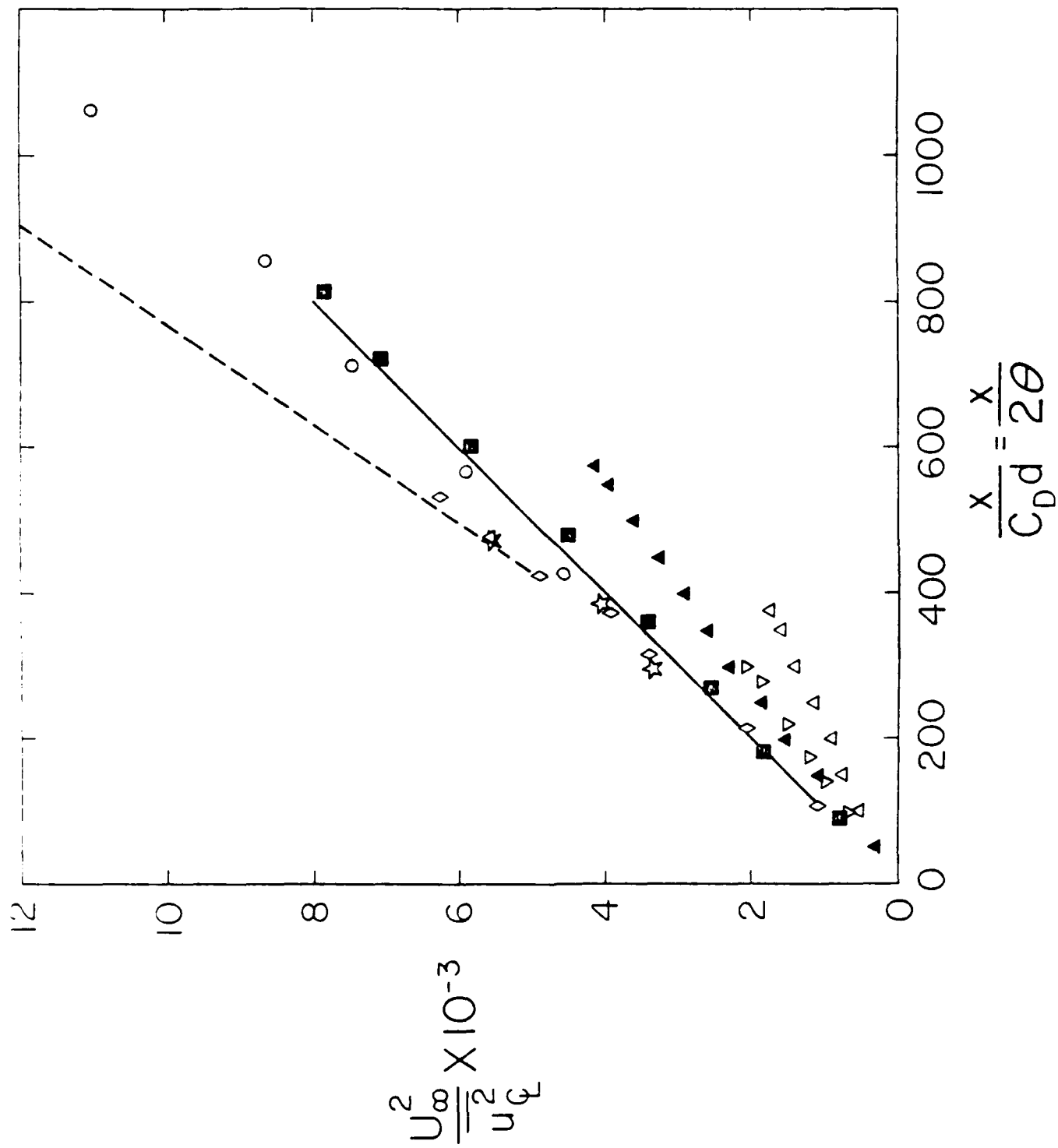


Figure 1.2

$$f(\eta) = \frac{U_{\infty} - U}{u_0}$$

$$\eta = \frac{y}{L_0}$$

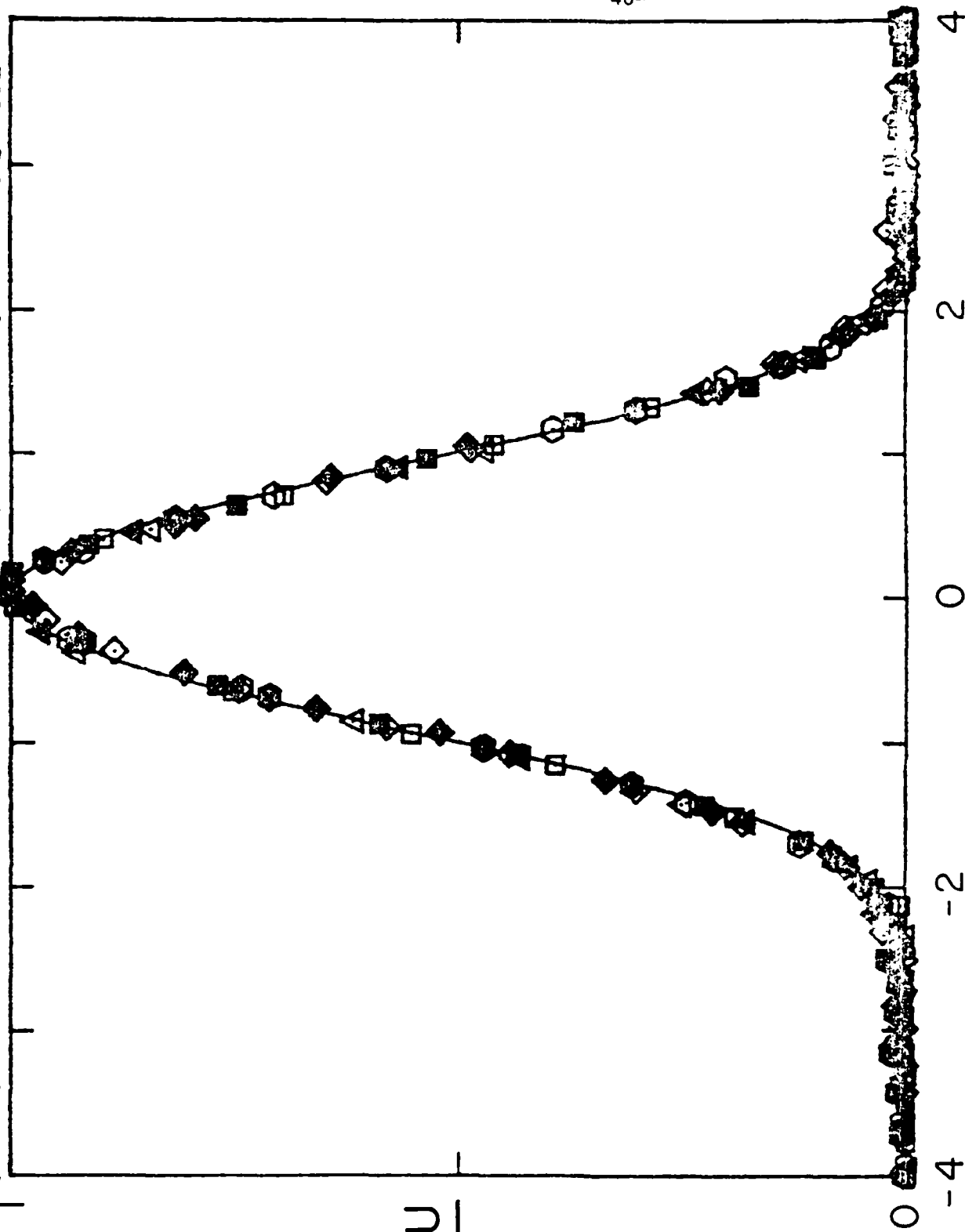


Figure 4.2.1

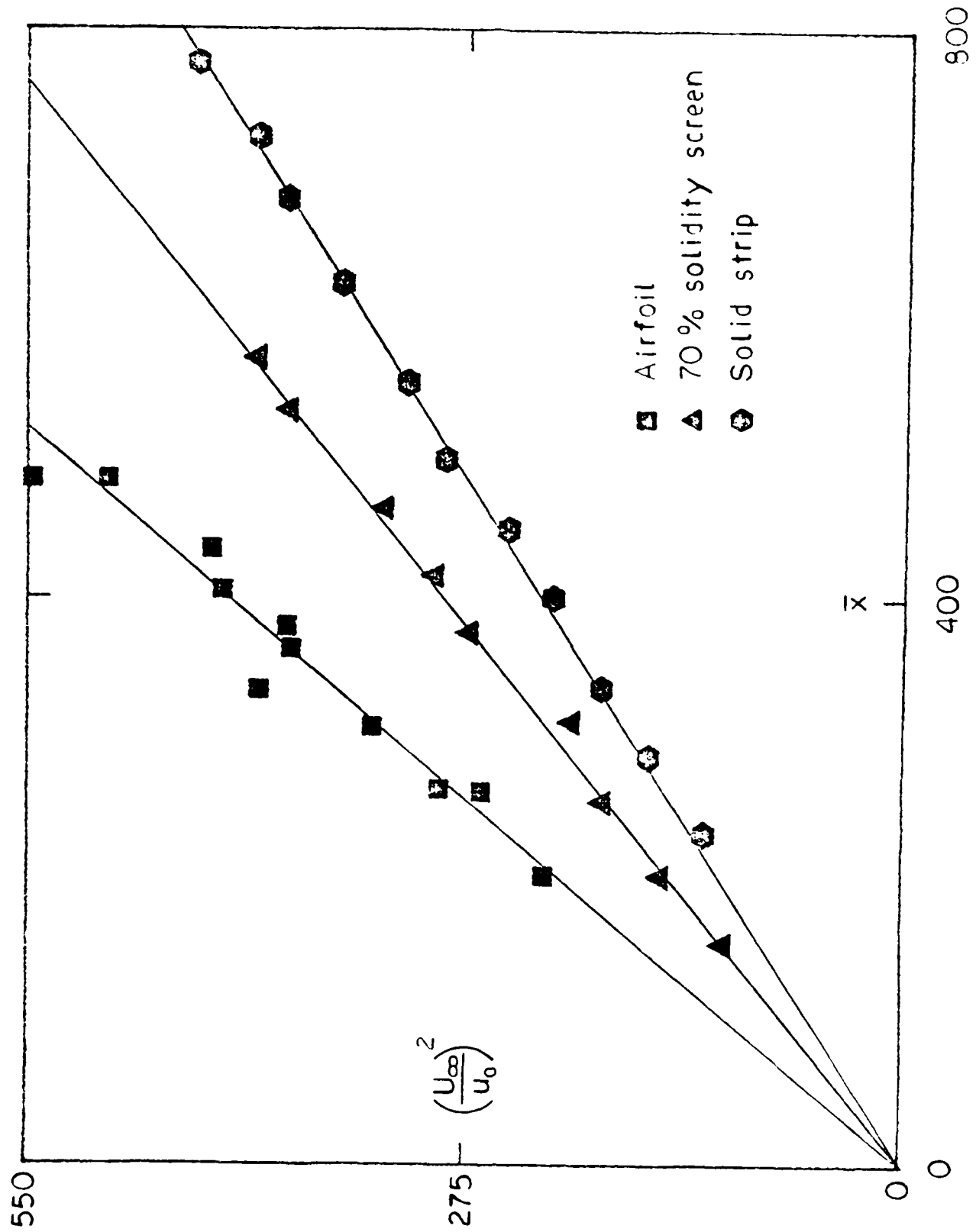


Figure 4.2.2

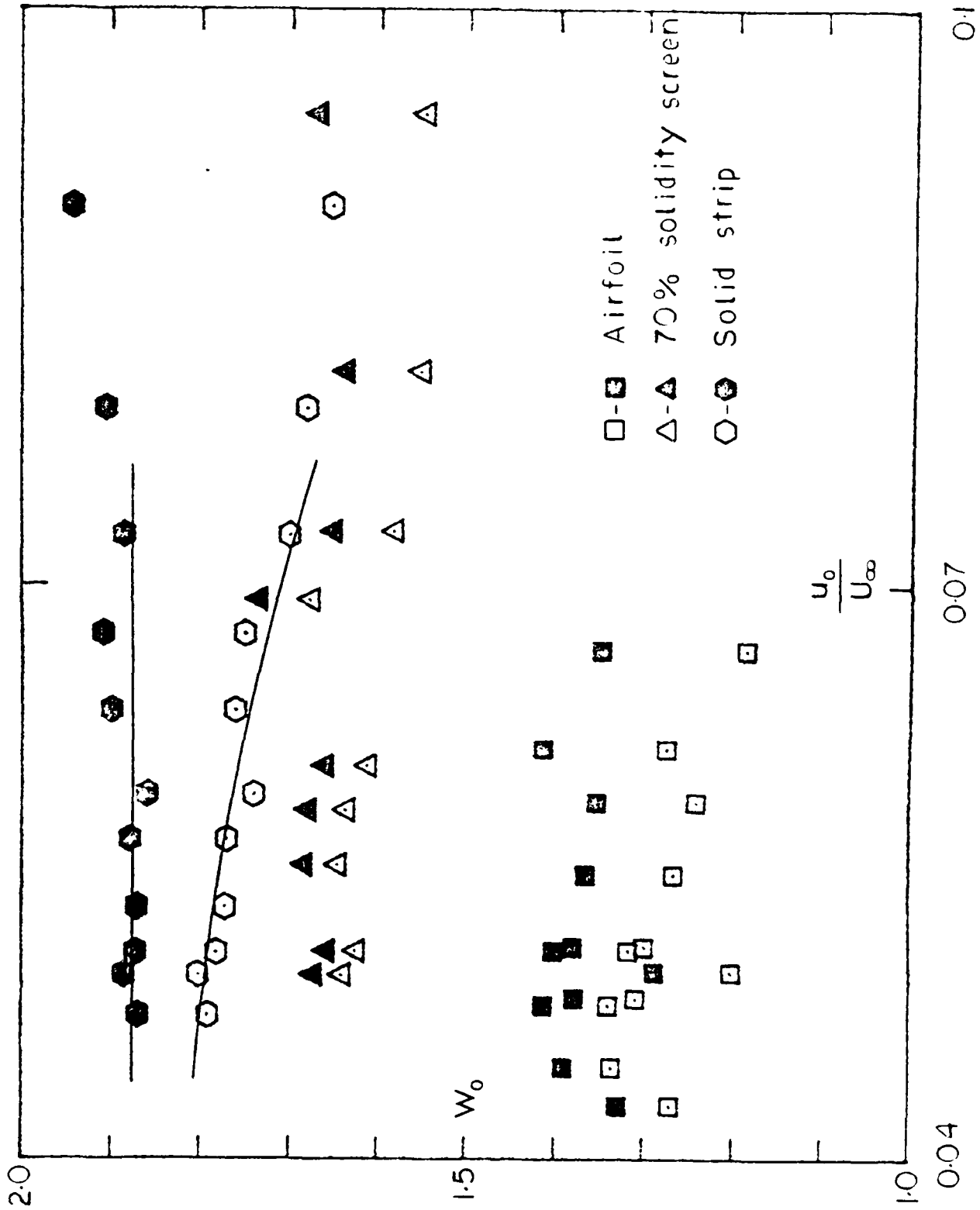


Figure 4.2.3

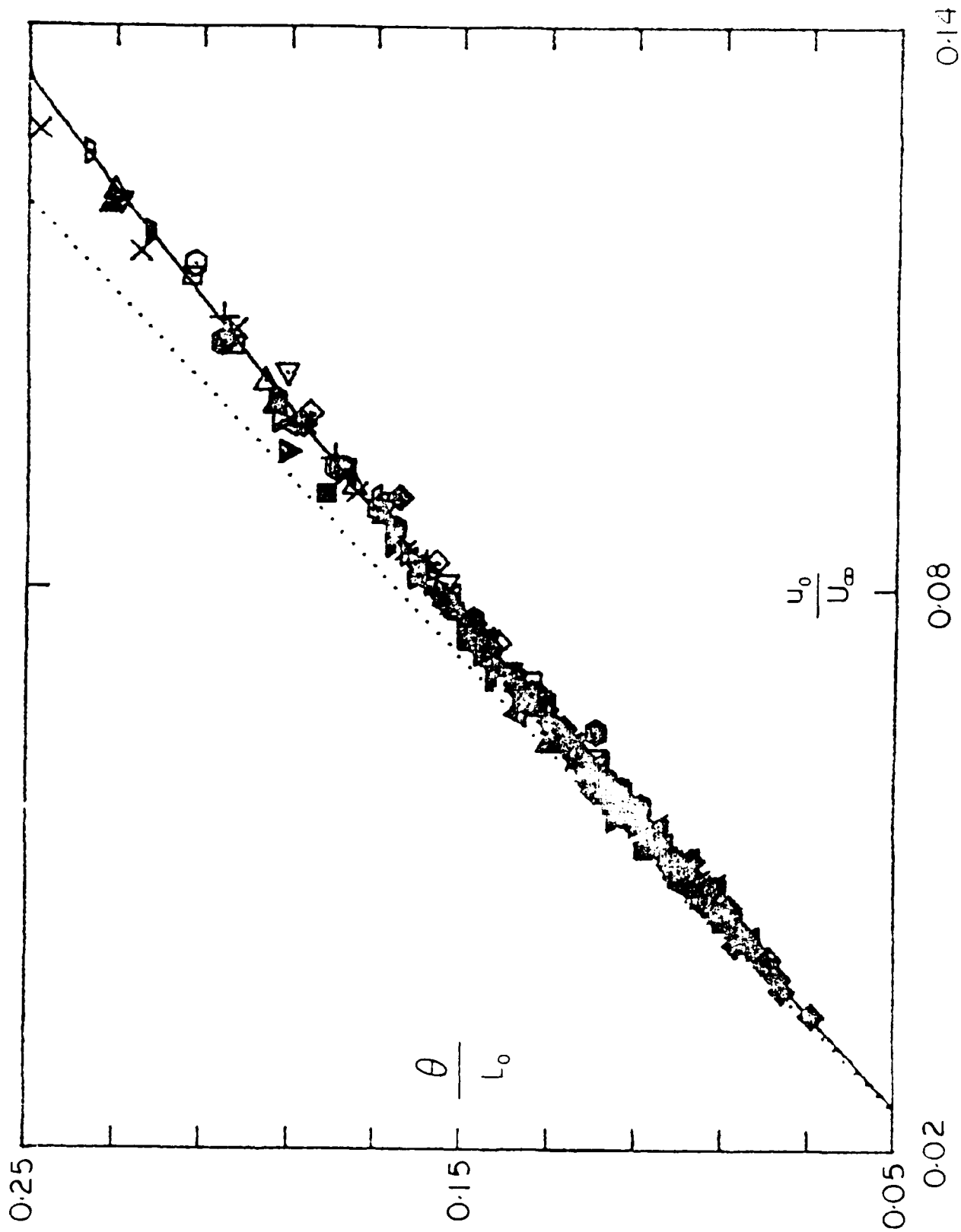


Figure 4.2.4

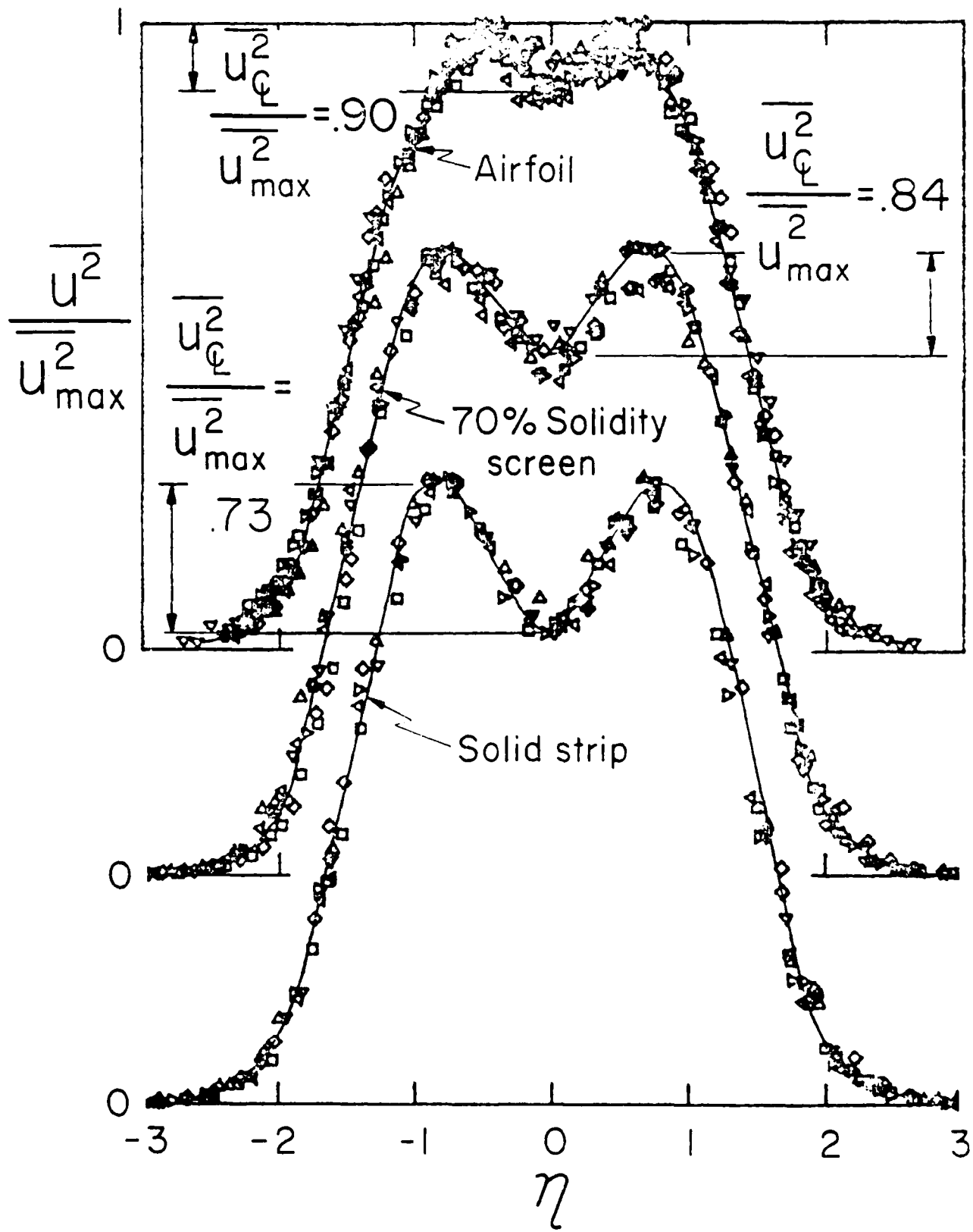


Figure 4.3.1

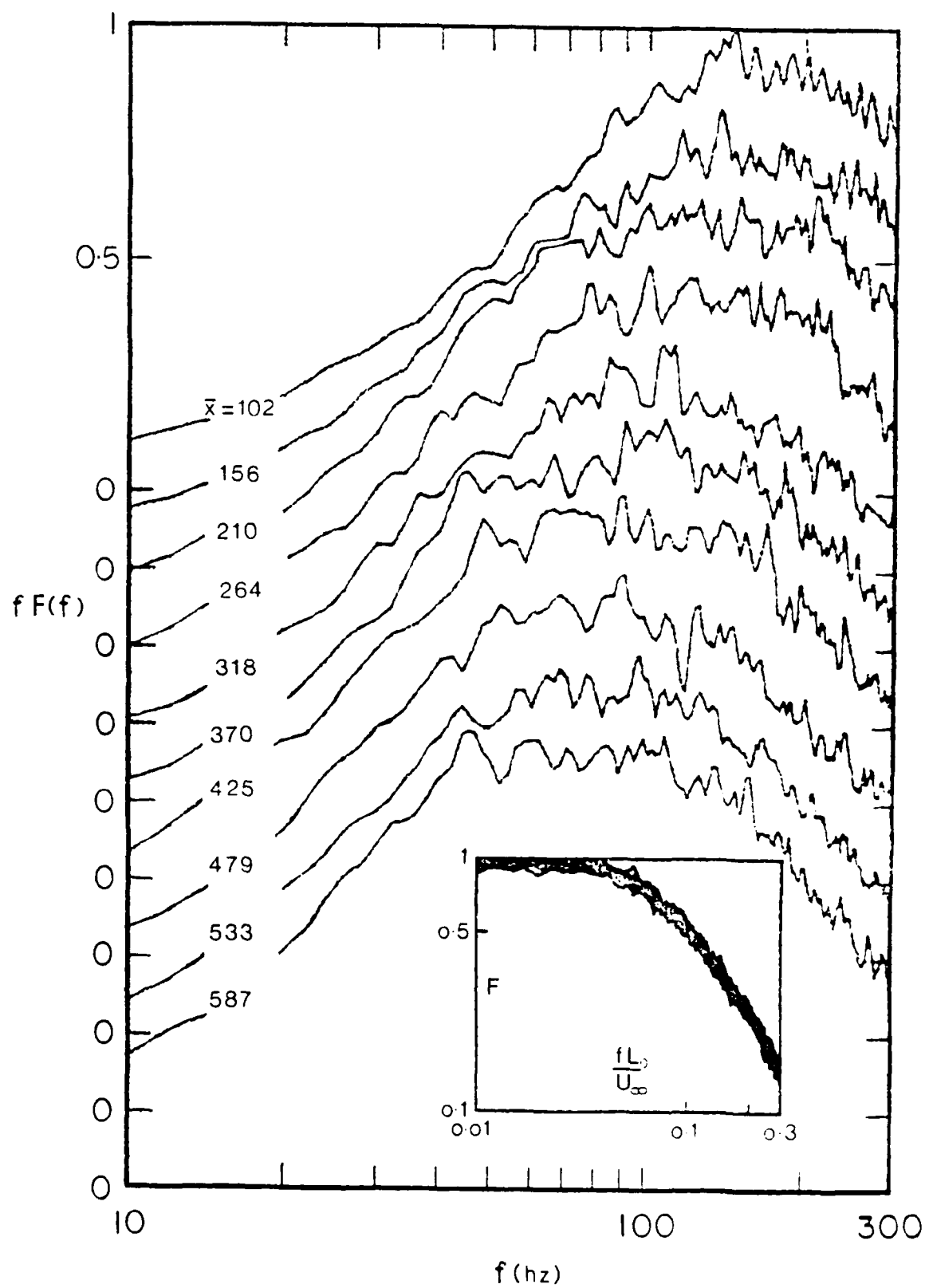


Figure 4.4.1

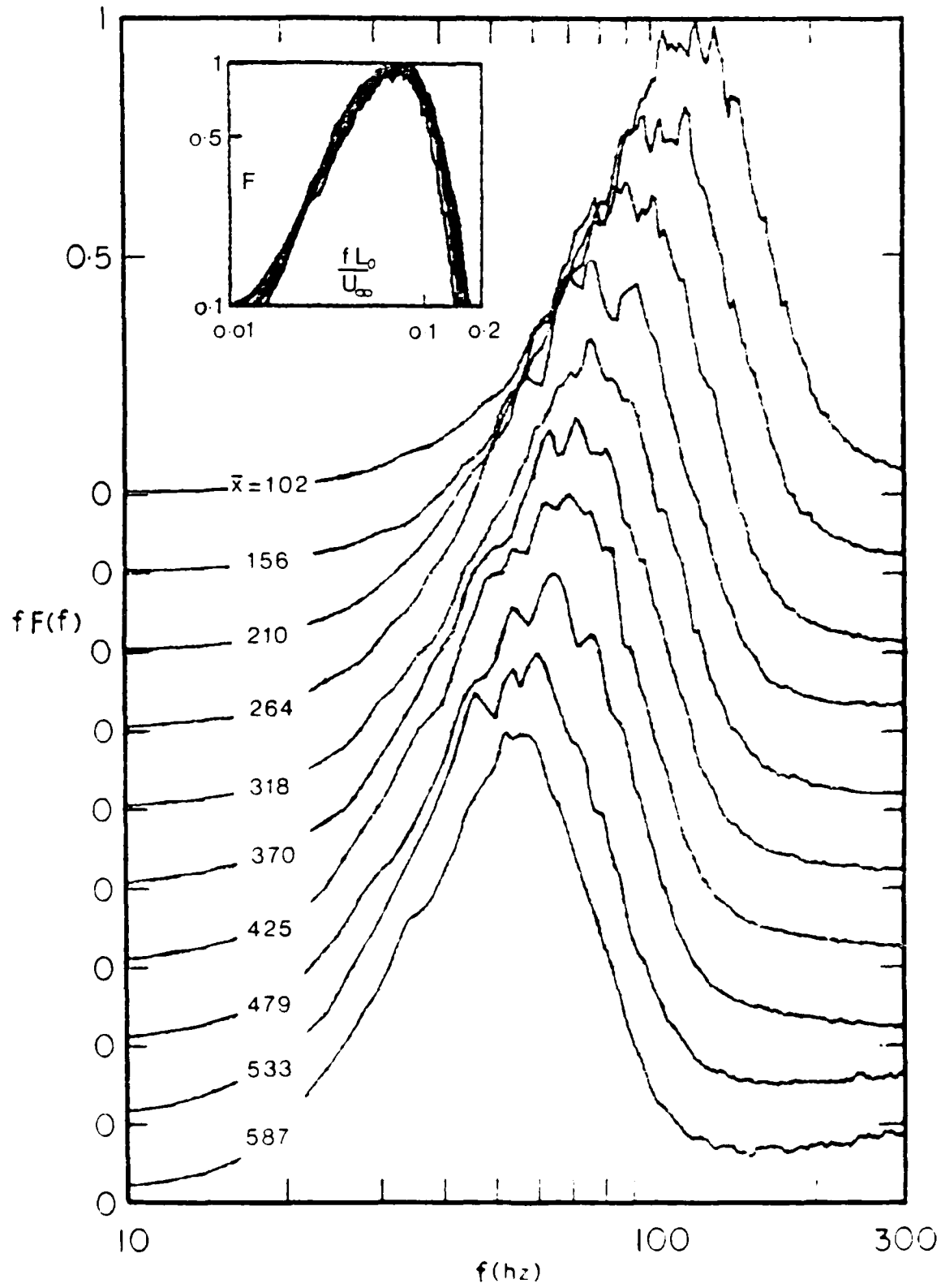


Figure 4.4.2

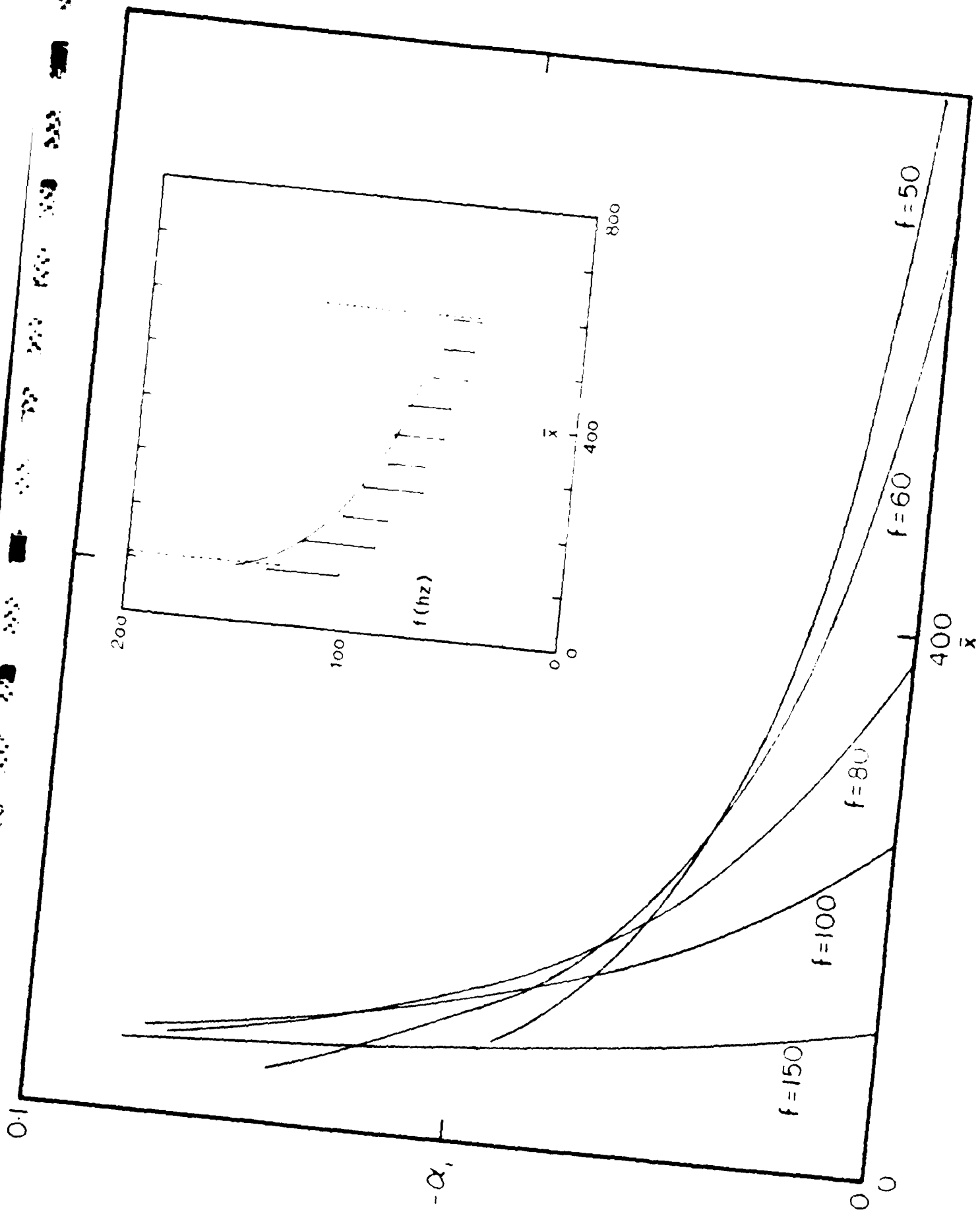


Figure 4.4.3

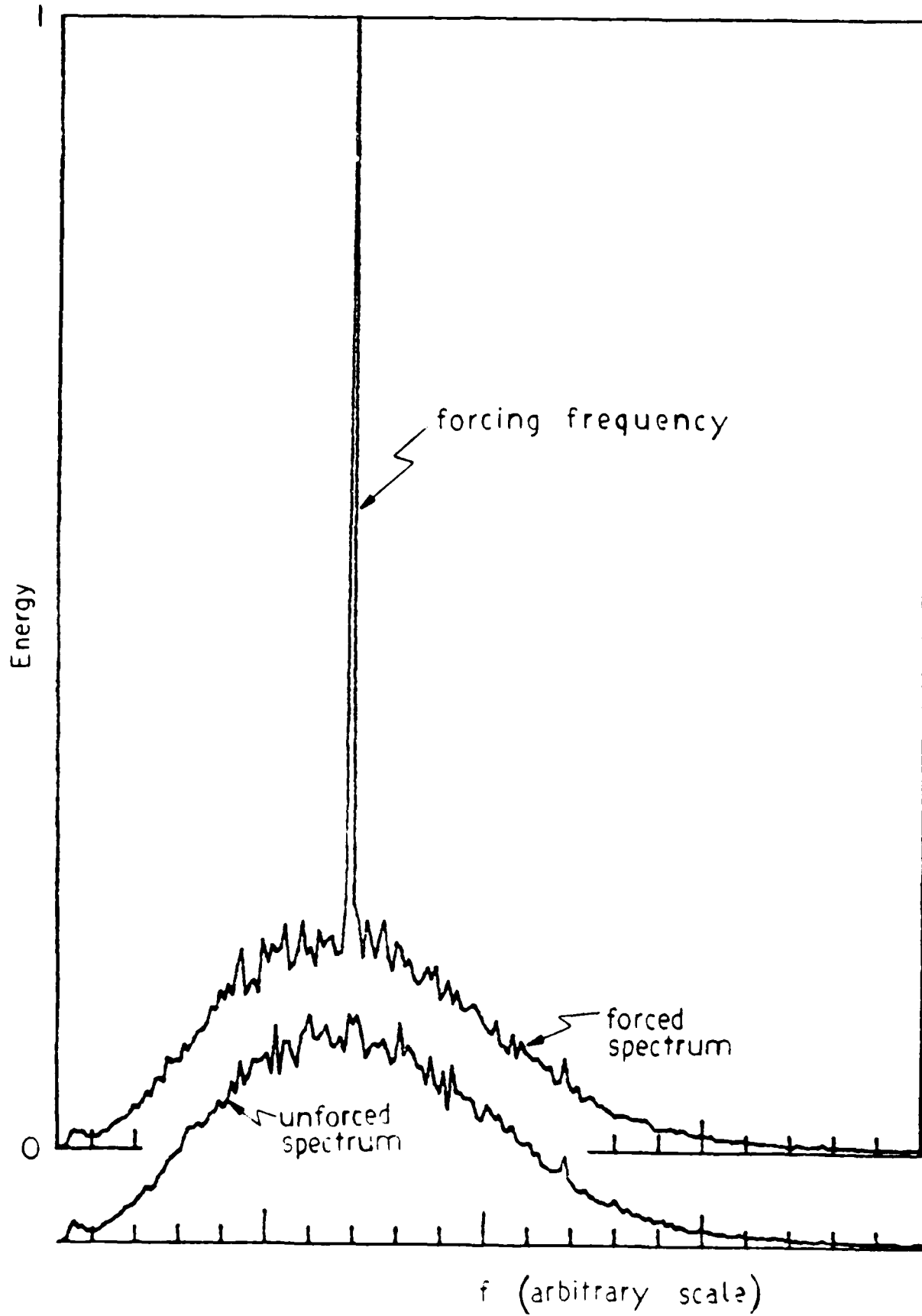


Figure 4.5.1

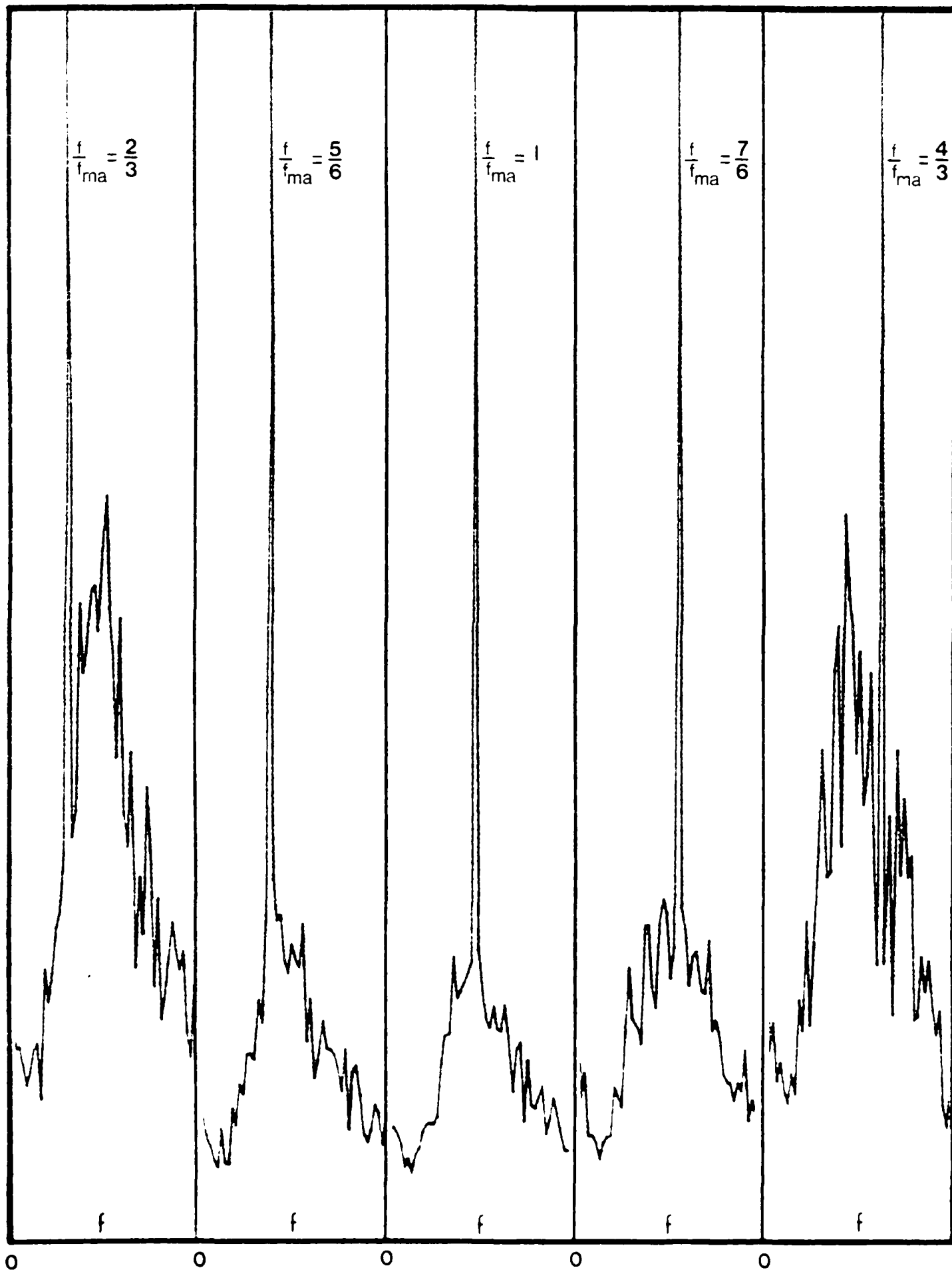


Figure 4.5.2

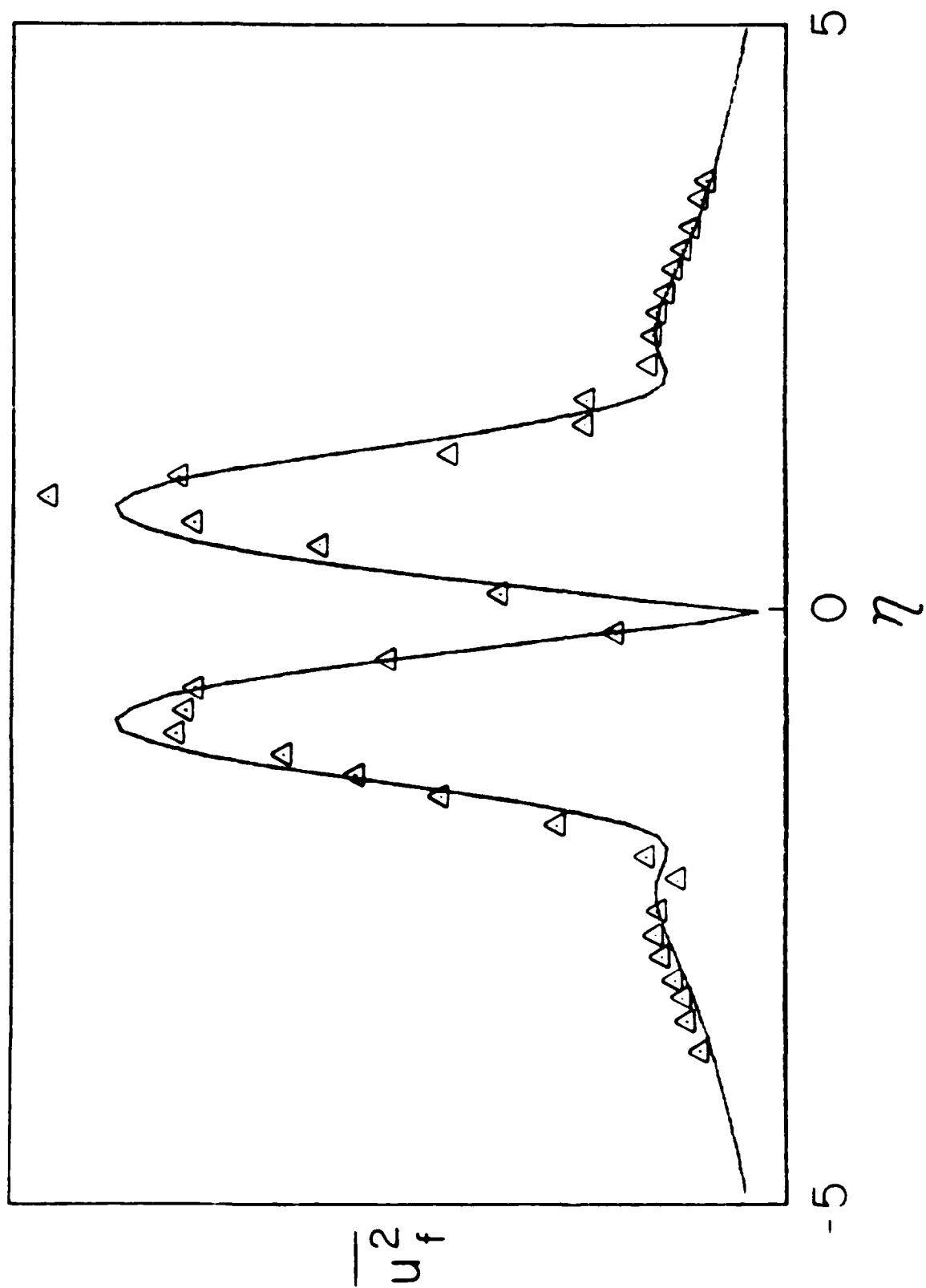


Figure 4.5.3

$$\frac{A(\bar{x})}{A(700)}$$

700 640 592 539 486 432 378 325

η

Figure 4.5.4

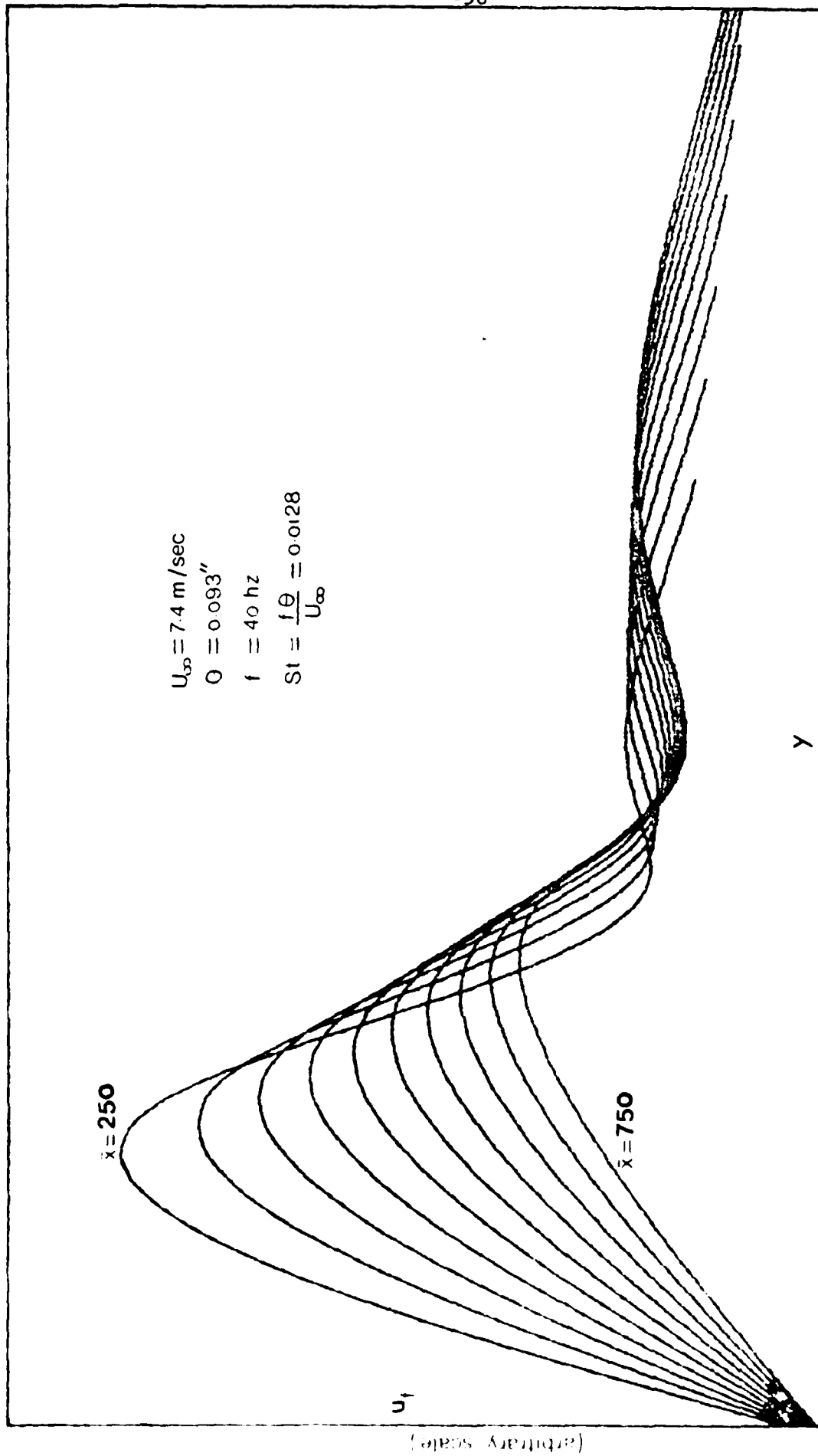


Figure 4.5.5

1.6

0.4

$$\frac{\Delta\varphi(\bar{x})}{\Delta\varphi(700)}$$

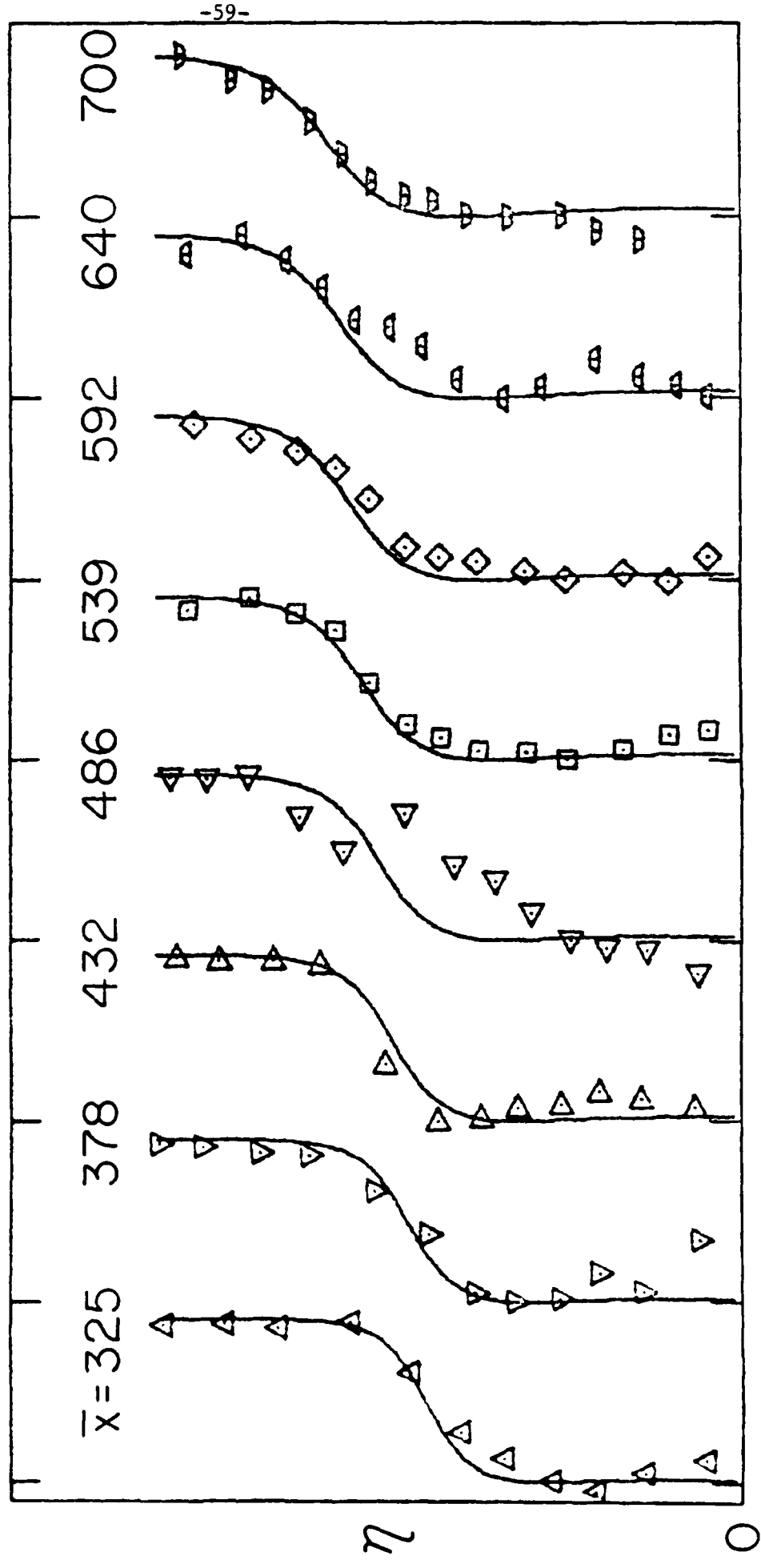


Figure 4.5.6

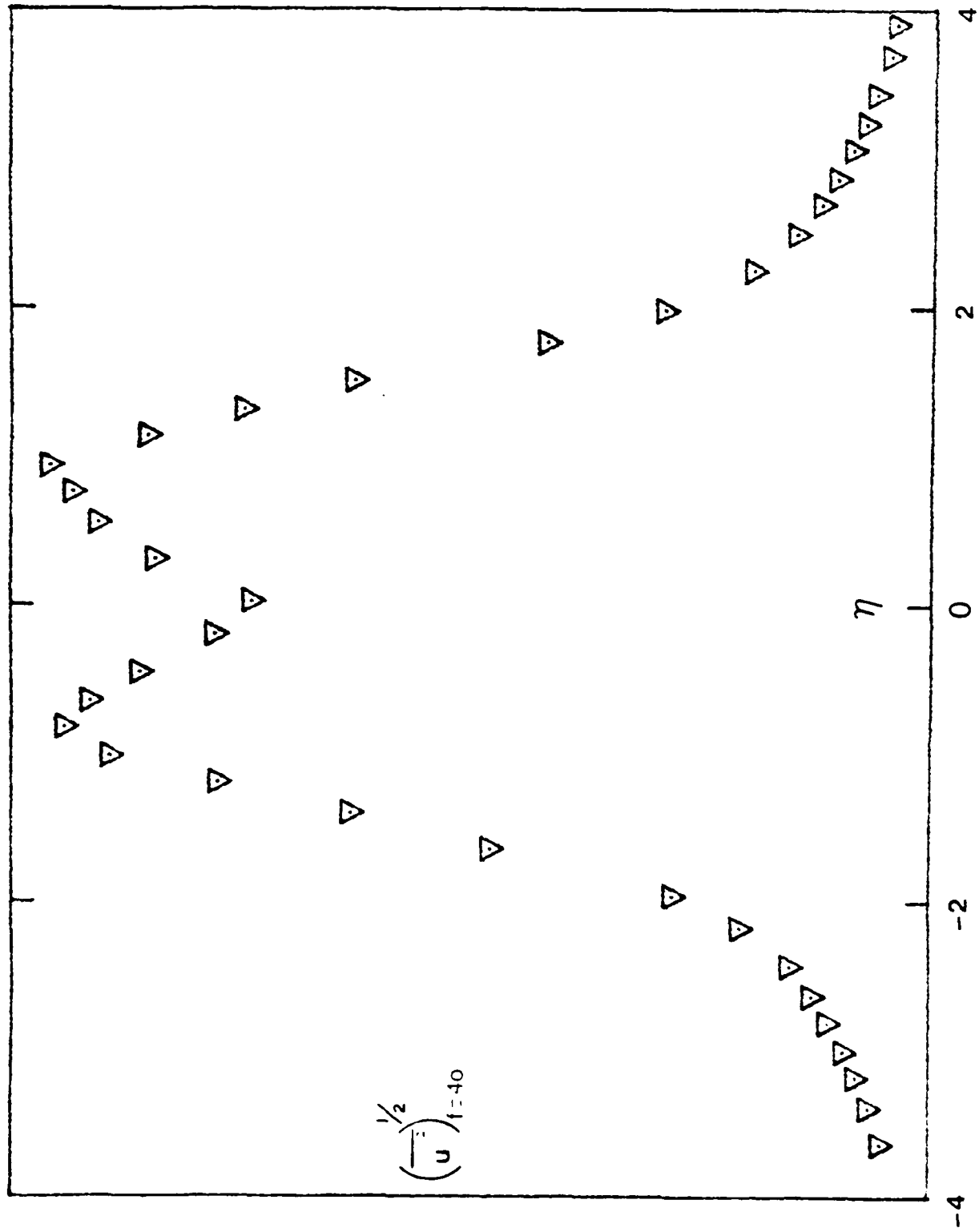


Figure 4.6.1

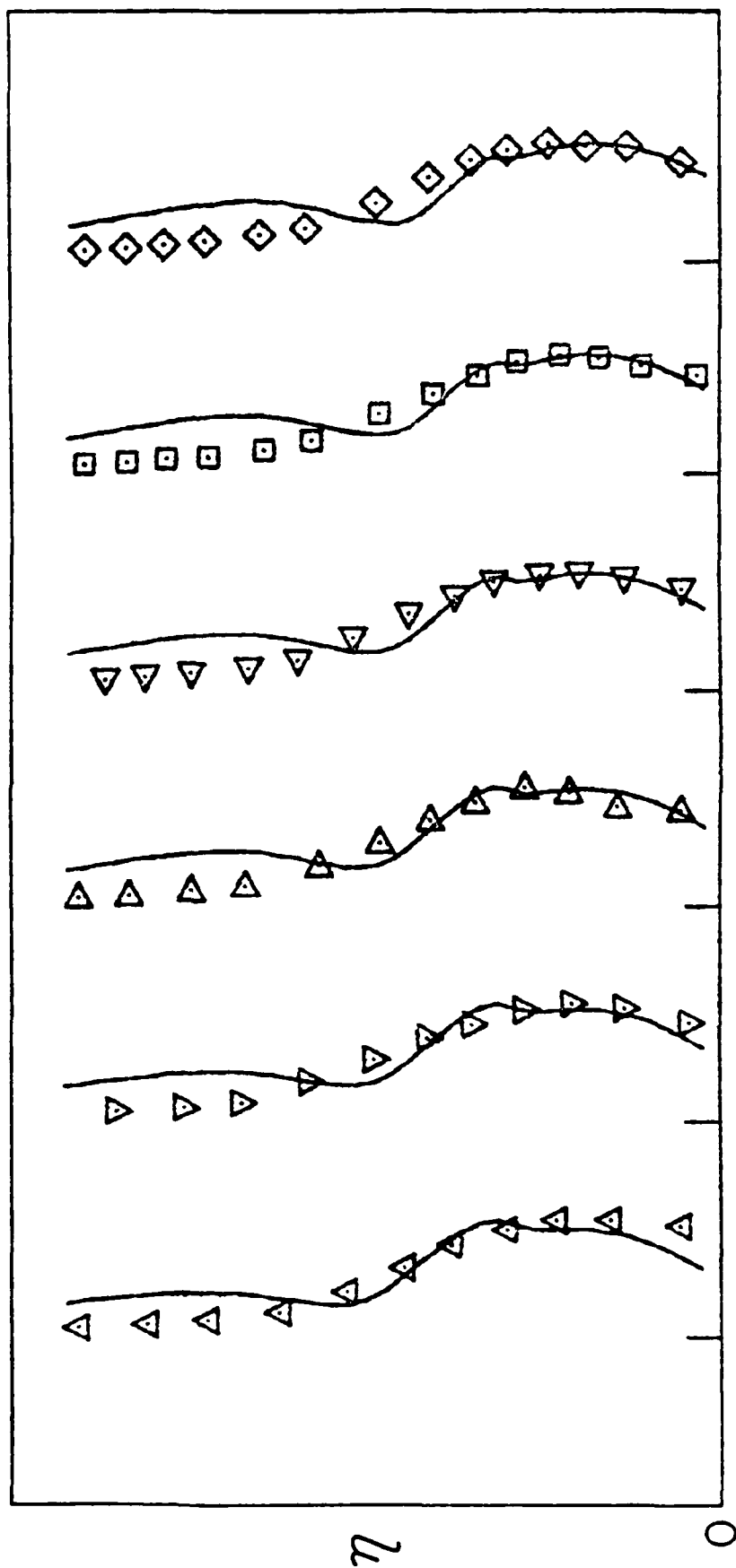
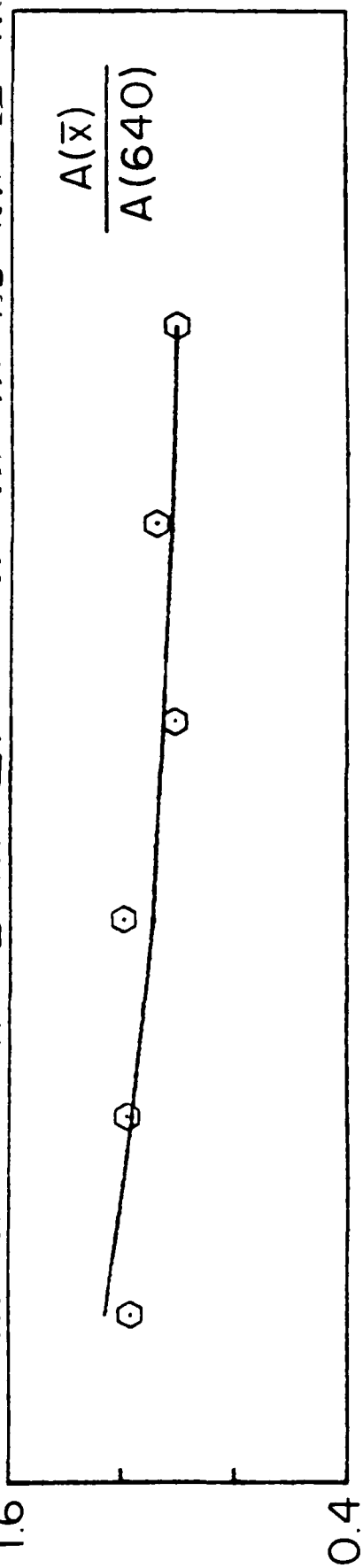


Figure 4.6.2



$\bar{x} \approx 400$

$\bar{x} \approx 600$

Figure 4.6.3



z

$x \approx 600$

flow

$x \approx 400$

Figure 4.6.4

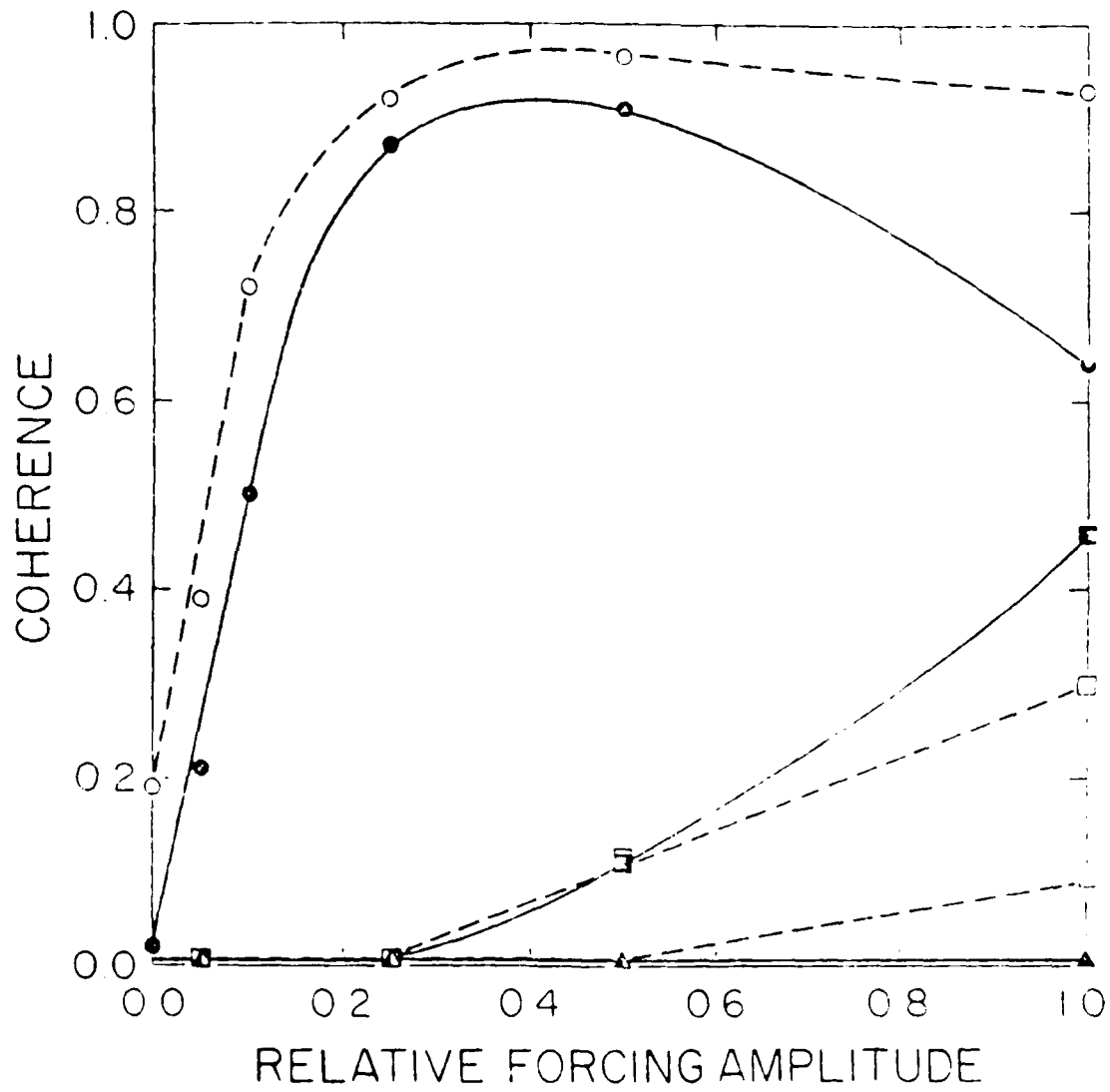


Figure 4.6.5

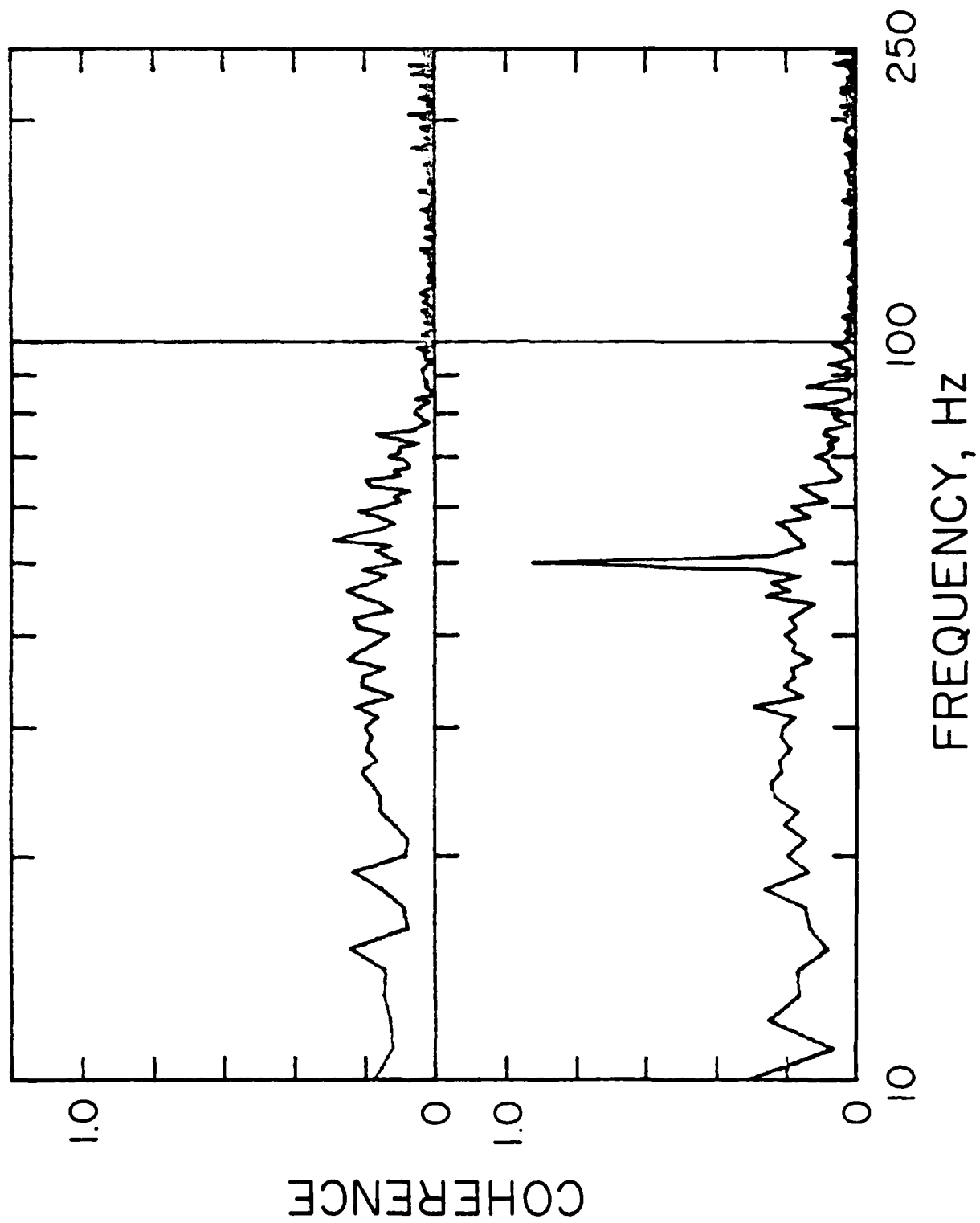


Figure 4.6.6

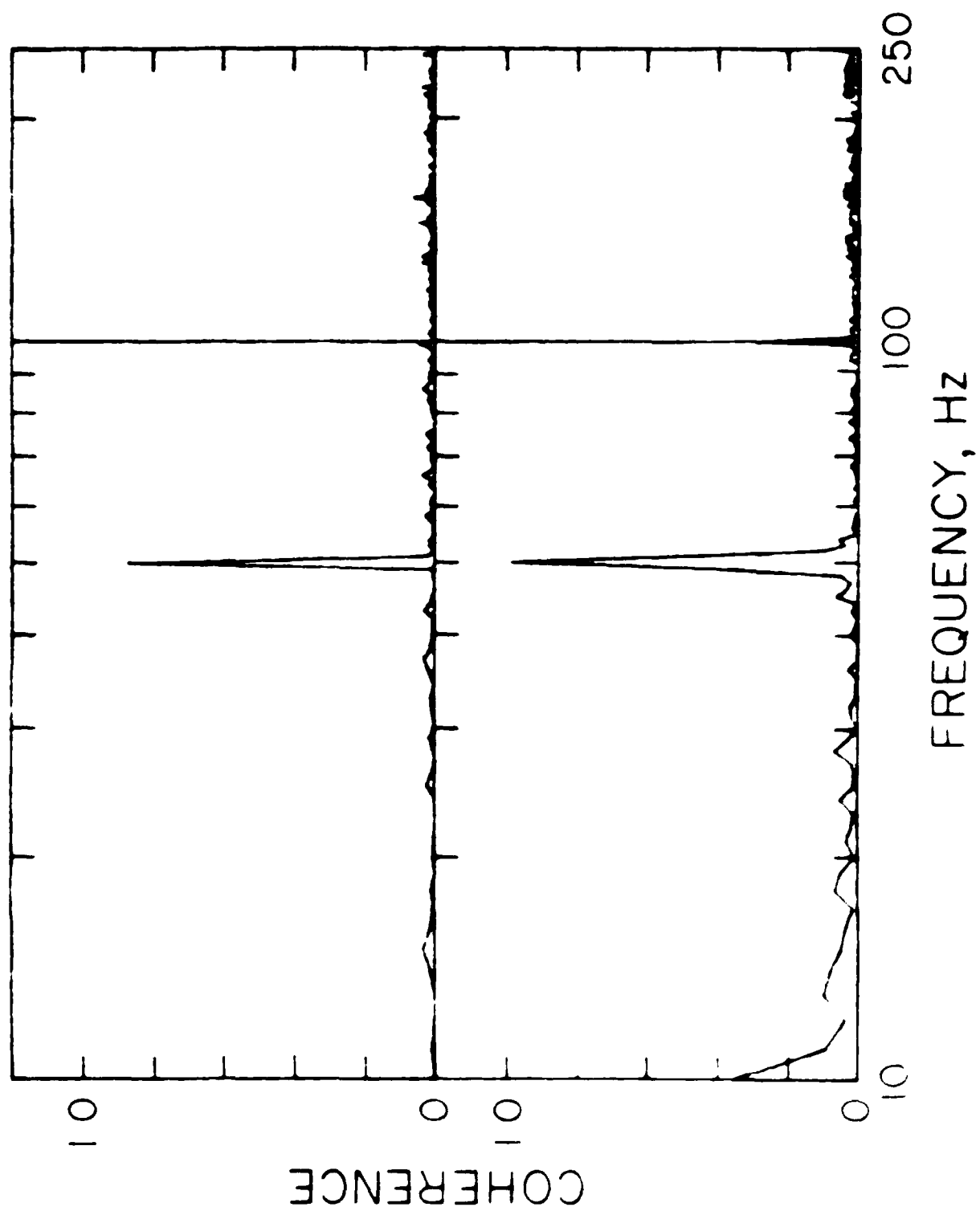
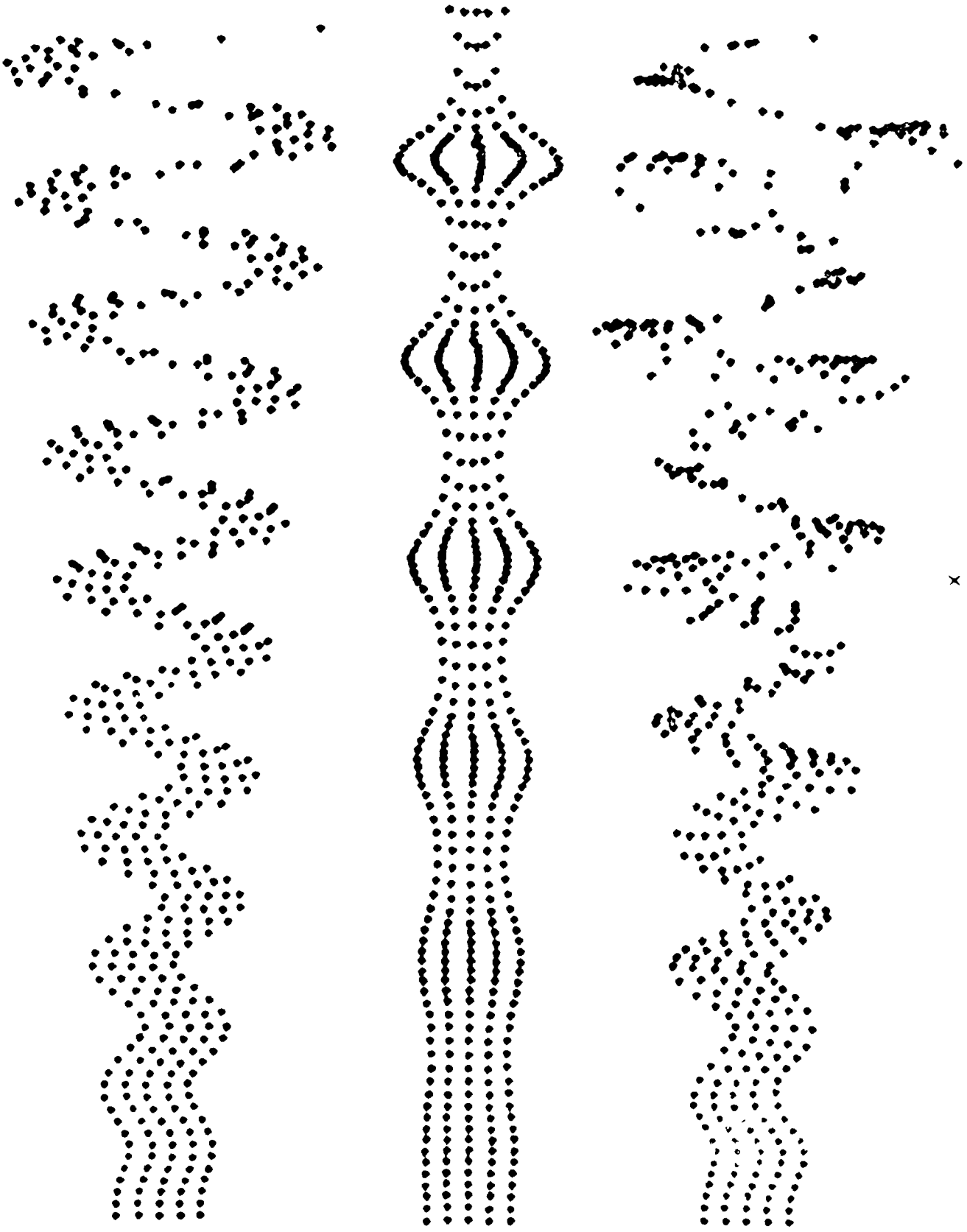


Figure 4.6

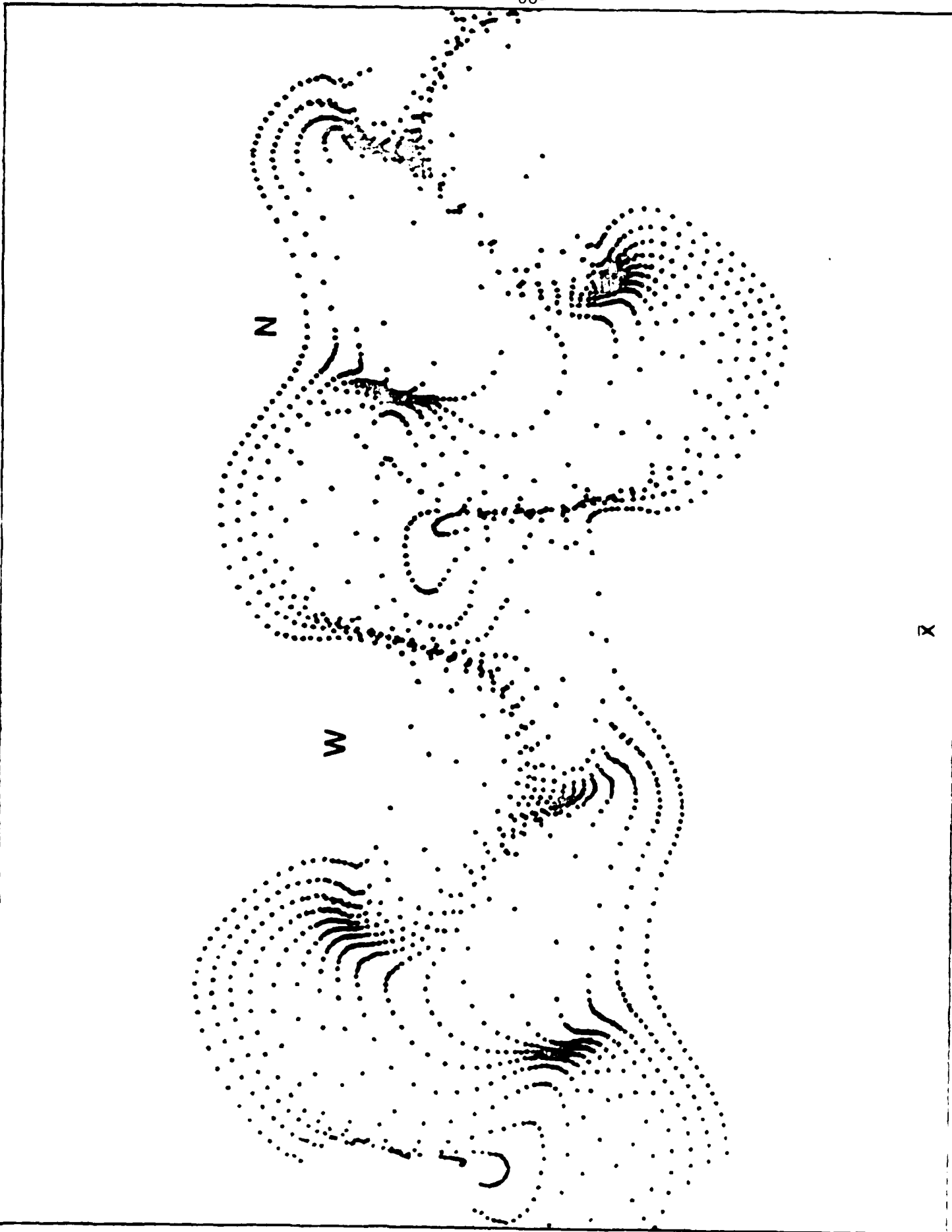
Figure 4.6.8

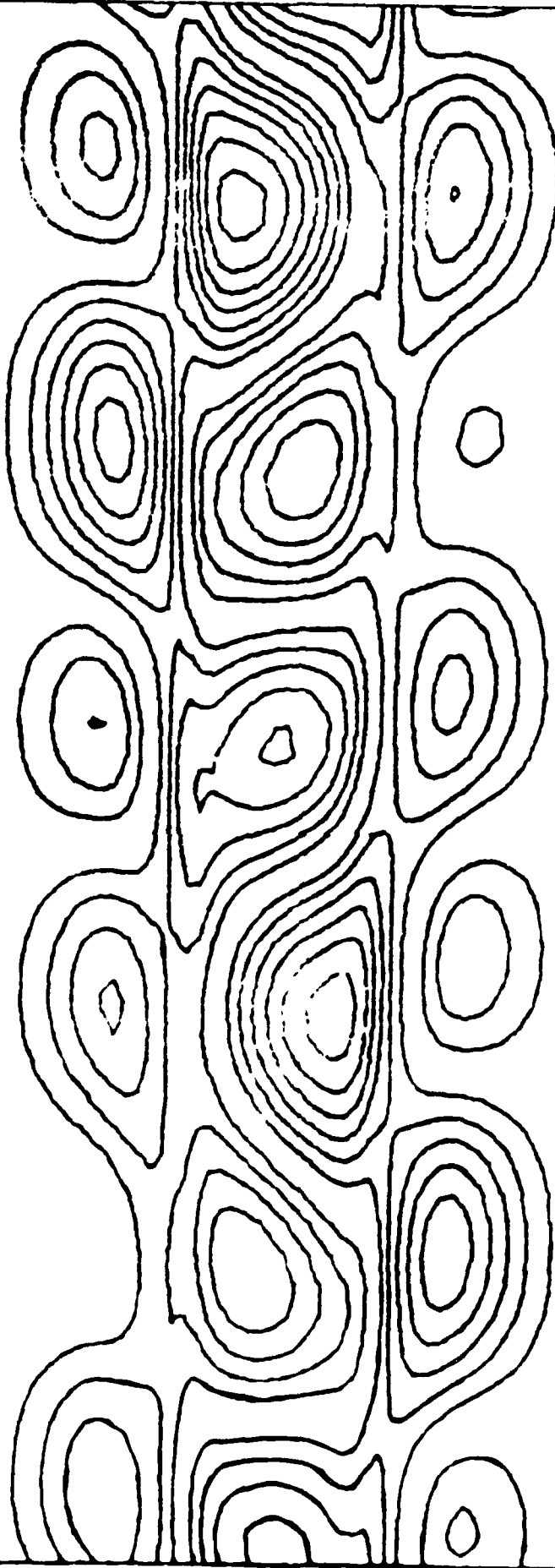
z "

x



5 10 15 20 25 30 35 40 45 50 55 60 65 70 75 80 85 90 95 100

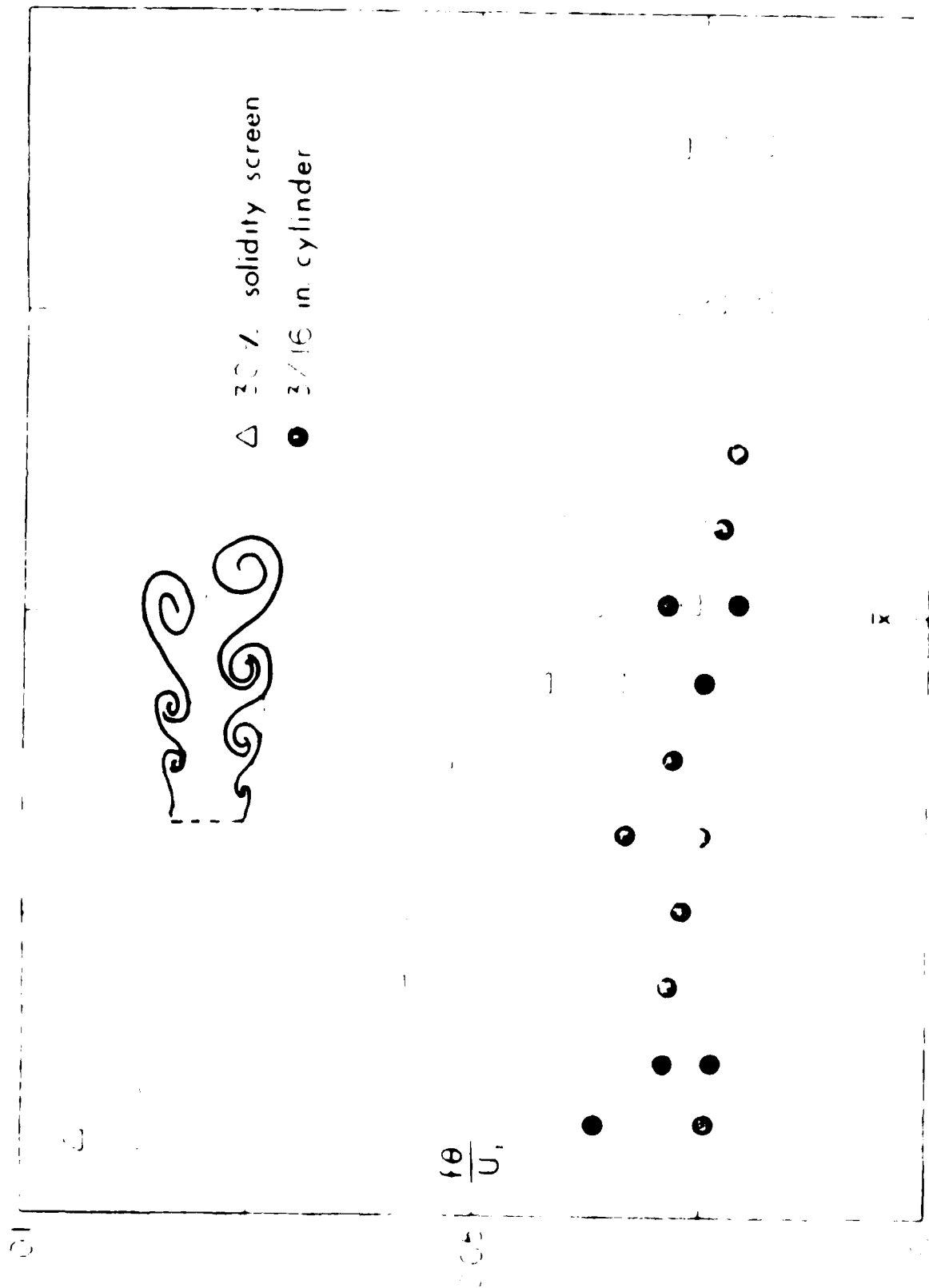


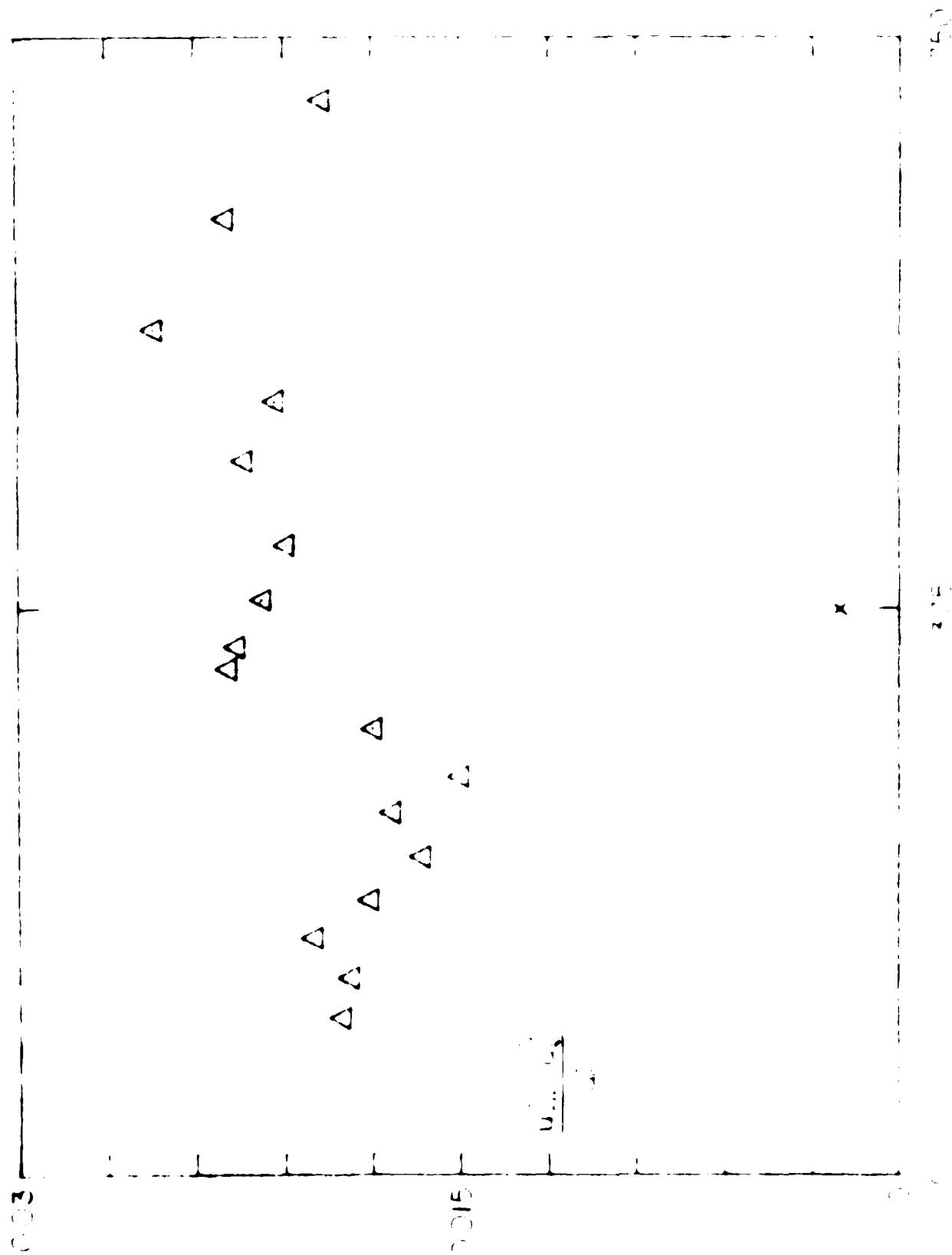


70

x

Figure 4.6.10





LIST OF TABLES

- 1 Summary of Wake Generators
- 2 Summary of Experimental Results on Wake Generators

Table 1. Boundary of Wake Generators

Remarks	0	mm
1/d=384 Drill Rod	640, 925, 1410	0.74
1/d=128 Drill Rod	933, 1990, 3200	2.23, 2.33, 2.64
1/d=96 Drill Rod	3220	2.64
Solidity		
Mech		
28 x 28	1980	2.32
40 x 40	2010	2.33
50 x 50	2040	2.39
-	1970	2.31
-73-		
Rounded leading edge; tapered to 1 mm	1035	2.36
Boundary layer on both sides tripped. Solid aluminum plate.		
Boundary layer tripped. Extruded aluminum tubing filled with sand	1900	2.23

Table 2. Summary of Experimental Results on Wake Generators

WAKE GENERATOR	U (m/s)	e (mm)	$\frac{x_0}{2e}$	W_0	Δ_0	$W_0 * \Delta_0$
3/16" Cylinder	14.5	2.33	-74	1.75	0.289	0.506
30% Solidity Screen	14.5	2.31	58	1.82	0.279	0.508
45% Solidity Screen	14.5	2.33	27	1.78	0.285	0.507
70% Solidity Screen	14.5	2.39	-21	1.67	0.302	0.504
Solid Strip 100% Solidity	14.5	2.31	-64	1.88	0.270	0.508
Symmetrical Airfoil	14.5	2.23	-43	1.35	0.377	0.509
Flat Plate	7.45	2.36	5	1.71	0.297	0.508
Flat Plate Flap Freq=50 Hz AMP = 0.2V	7.45	2.36	48	1.48	0.344	0.509
Flat Plate Flap Freq=50 Hz AMP = 0.3V	7.45	2.46	61	1.32	0.382	0.504
Flat Plate Flap Freq=20 Hz AMP = 0.5V	7.45	2.40	48	1.57	0.323	0.507
3/16" Cylinder (Chapman 1982)	20.7	2.54	-100	1.74	0.288	0.501
1/16" Cylinder	21.4	0.737	-170	1.77	0.285	0.504
1/16" Cylinder	14.5	0.737	-130	1.74	0.287	0.500

END

5-87

DTIC